COMMISSION D: Electronics and Photonics
(November 2013 - October 2016)

Edited by Katsutoshi Tsukamoto, Osaka Institute of Technology

---

Electronics and Photonics cover huge scientific and technological fields. Among them, in this report, we have selected several important topical areas, where in particular Japanese leading researchers have actively contributed between 2013 and 2016. They overviewed recent remarkable advances in their specialized areas.

The following is a list of areas that the chapter editor has taken up.

D1. Quantum Cascade Lasers and Optical Antennas
Kenichi Kasahara
Ritsumeikan University

D2. Current-Injection Terahertz Lasing in a Distributed-Feedback Dual-Gate Graphene-Channel Transistor
Taiichi Otsuji
Tohoku University

D3. Terahertz Photonic Crystals
Masayuki Fujita
Osaka University

D4. THz-Wave Emitters and Detectors Based on Diode Technology
Hiroshi Ito
Kitasato University

D.5 Millimeter-wave and submillimeter-wave antennas in standard CMOS technology
Eiichi Sano
Hokkaido University

D6. Space-Division-Multiplexed Optical Fiber Transmission
Hiroyuki Toda
Doshisha University

D7. Recent research trends in optical access network technologies
Jun-ichi Kani
NTT Corporation

D8. Optical Access Networks for broadband IoT services
Naoto Yoshimoto
Chitose Institute of Science and Technology

D9. Construction of resilient cyber physical system based on ICT
Katsumi Iwatsuki
Tohoku University

D1. Quantum Cascade Lasers and Optical Antennas

Kenichi Kasahara

Ritsumeikan University

Significant progress in mid-infrared distributed-feedback quantum cascade lasers (QCLs) capable of continuous-wave operation above room temperature has allowed for the monitoring of trace gases relating to environmental and energy issues. To extend the application of QCLs, a modular waveguide mounting accessory specifically designed for on-chip thin-film GaAs/AlGaAs waveguides was reported [1]. GaAs slab waveguides with dimensions of 5 × 10 mm of different thickness (6 and 10 μm) were combined with a tunable QCL providing a wavelength range of 5−11 μm (1925−885 cm^{-1}) within a single collimated beam serving as evanescent field sensing transducers in lieu of conventional attenuated total reflection crystals. The waveguide mount was designed such that modular adaptation to any infrared optical assembly ensuring precise self-realignment was enabled. The sensor response to 50 μL of ammonium perchlorate solutions with concentrations of 0.01, 0.05, 0.1, 0.5, and 1 M using a 10 μm, and for comparison, a 6 μm thick GaAs thin-film waveguide was compared to results recorded via a Fourier transform infrared (FTIR) spectrometer. The QCL-based measurements revealed comparable results to conventional FTIR-based studies. The 6 μm waveguide provided a higher sensitivity in contrast to the 10 μm structure, which was attributed to the enhanced intensity of the evanescent field with increased mode confinement. However, it was found that the overall energy throughput was approximately ten times lower for 6 μm waveguides compared to the 10 μm structures, because the coupling efficiency into the waveguide was reduced at smaller waveguide dimensions.

On the other hand, the progress towards terahertz QCLs has been made since their birth in 2002 [2], and terahertz QCLs can now deliver milliwatts or more of continuous-wave coherent radiation throughout the terahertz range. However, it is still a challenge to increase their operating temperatures. One approach to overcome this problem is to use the Cherenkov difference-frequency phase-matching scheme. Intracavity difference-frequency generation in mid-infrared QCLs with a dual-upper-state (DAU) active region was used to get terahertz oscillation [3]. DAU active region design was theoretically expected to produce larger optical nonlinearity for terahertz difference-frequency generation, compared to the active region designs of the bound-to-continuum type used previously. Fabricated buried heterostructure devices with a two-section buried distributed feedback grating and the waveguide designed for Cherenkov difference-frequency phase-matching scheme operated in two single-mode mid-infrared wavelengths at 10.7 μm and 9.7 μm and produced terahertz output at 2.9 THz. The mid-infrared to terahertz conversion efficiency was 0.8 mW/W^2 at room temperature.

To broaden the application of QCLs, photo-detectors exhibiting both high-sensitivity and high-speed are needed in the mid-infrared range. Optical antennas generate optical hotspots, and enhance local field intensity near the antenna, thereby allowing for efficient photon harvesting. Thus, sufficient absorption is obtainable even from a thin absorption layer, and it is possible that a combination of optical antennas and a thin photo-absorption layer leads to the achievement of high-performance mid-infrared detectors with high-sensitivity and quick response times. Field intensity becomes large near an antenna, and decreases rapidly with increasing distance from it. Accordingly, it is necessary to know the increased field distribution of the antenna in the vertical direction for designing mid-infrared photo-detectors equipped with antennas. The finite-difference time-domain (FDTD) method is a powerful tool for use in the design of optical devices, which can calculate electric fields in the depth direction. However, it is still necessary to evaluate the appropriateness of the obtained results in a practical manner, because FDTD simulation necessitates the frequency dispersive nature of media in an analytical domain and very fine discretization in space in order to correctly predict the electromagnetic distribution, particularly, in the case of optical antennas including metals. The field enhancement of the antenna can be measured by observing a reflection or transmission spectra through a micro FTIR spectrometer. Local information on the field enhancement is also available if one uses a scattering near-field microscopy (s-SNOM). However, such measurements alone are insufficient to ascertain the distribution of field enhancement normal to an antenna plane.

To this end, a thin Al_2O_3 layer was deposited on a Si substrate through atomic layer deposition (ALD) with thickness being controlled to an accuracy of ~1 nm, and dumbbell-shaped slot antennas (DSAs) were fabricated on this [4]. By observing the spectral magnitude dependence of the SiO_2 layer, which was naturally formed on the Si layer, on the Al_2O_3 thickness, it was possible to actually gain an understanding of the distribution of enhanced electric field parallel to the substrate surface in the depth direction. Fig. 1 shows normalized reflectivity vs. wavenumber for antenna arrays on an Al_2O_3/Si substrate. The thicknesses of the ALD-made Al_2O_3 were 20, 40, and 60 nm. The reflectivity-increase region of 1050~1250 cm^{-1} corresponding to the restrahlen band of native Si oxide weakened as the Al_2O_3 was deposited and the thickness was increased. The band almost disappeared for a 60-nm Al_2O_3, meaning that the electric field in a natural SiO_2 layer weakened with increases in the thickness of Al_2O_3. Reflectivity increase around 750~1100 cm^{-1} was due to the restrahlen band of Al_2O_3 layer.

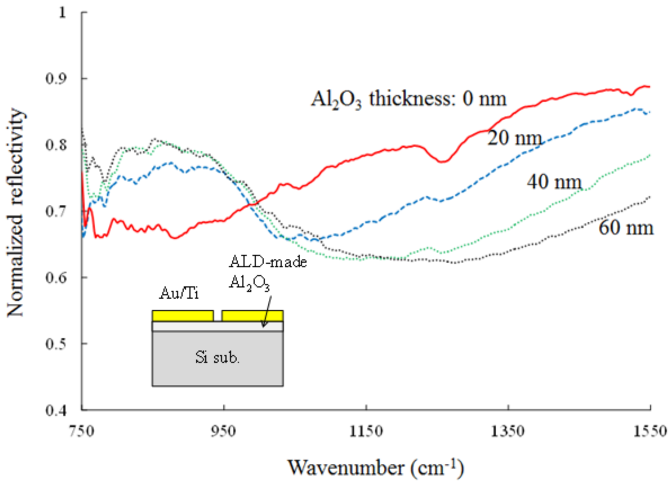

Fig. 1 Normalized reflectivity vs. wavenumber for antenna arrays on an Al_2O_3/Si substrate. The lengths and gap width of a DNA were 1.5 μm and 0.1 μm, respectively. The thicknesses of the ALD-made Al_2O_3 were 20, 40, and 60 nm [4].

Experimental results were compared with FDTD calculation. Measured results were in reasonable quantitative agreement with the FDTD calculation, but strictly speaking, it was found that there were some points which were unaccountable for from the simulation, which wasn’t universal in predicting the electromagnetic distribution in optical devices, particularly with antennas. Combing the FDTD method with the ALD technique allows for more accurate analysis of field enhancements in the perpendicular direction.

Next, this technique was applied to investigate the distribution of enhanced electric field normal to the substrate surface in the depth direction to develop high-performance mid-infrared detectors by combining the field enhancement effect of an optical antenna and intersubband transitions in quantum wells. Intersubband transitions occur as electromagnetic waves with an electric field component perpendicular to the quantum well layers are irradiated. Circular slot antennas were formed on an ALD-made Al_2O_3/SiC substrate. Surface phonon polariton (SPhP) signals originating from the SiC substrate [5] were used to estimate the electric field perpendicular to the substrate by varying the Al_2O_3 thicknesses. SPhPs are bound to the interface between Al_2O_3 and SiC, and possess s-polarization. Thus, it was possible to grasp the in-depth distribution of electric fields increased by optical antennas by changing the thickness of the Al_2O_3 spacer layer (Fig. 2). The knowledge obtained in this study is available for designing high-performance mid-infrared detectors with high-sensitivity and quick response times.

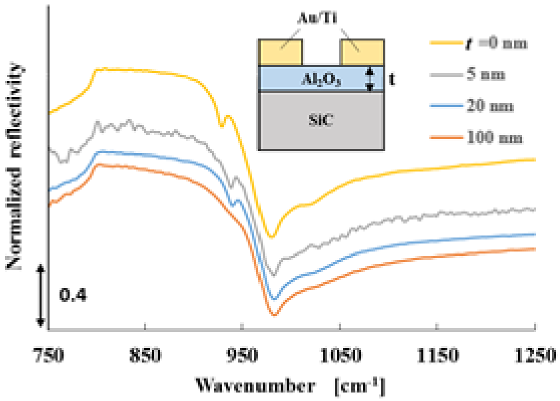

Fig. 2 Normalized reflectivity of circular-slot antenna array on Al_2O_3/SiC substrate when the thickness of Al_2O_3 was changed. The diameter of the antenna was 6 μm. When t = 0 nm, it was found that a decrease in reflectivity at 929 cm^{-1}, caused by SPhP, appeared among the Restrahlen band of SiC ranging from 800 to 970 nm. This dip almost disappeared when t = 100 nm, because the interface of Al_2O_3 and SiC was distant from the antenna, and field enhancement was weak [6].

References

[1] M. Sieger, J. Haas, M. Jetter, P. Michler, M. Godejohann, and B. Mizaikoff, “Mid-infrared spectroscopy platform based on GaAs/AlGaAs thin film waveguides and quantum cascade lasers,” Anal. Chem., Vol. 88, pp. 2558−2562, 2016.

[2] R. Köhler, A. Tredicucci, F. Beltram, H. E. Beere, E. H. Linfield, A. G. Davies, D. A. Ritchie, R. C. Iotti, and F. Rossi, “Terahertz semiconductor-heterostructure laser,” Nature, Vol. 417, pp. 156-159, 2002.

[3] K. Fujita, M. Hitaka, A. Ito, T. Edamura, M. Yamanishi, S. Jung, and M. A. Belkin, “Terahertz generation in mid-infrared quantum cascade lasers with a dual-upper-state active region,” Appl. Phys. Lett., DOI: 10.1063/1.4923203, 2015.

[4] Y. Nishimura, T. Kawano, Y. Kunichika, K. Kasahara, T. Yaji, N. Ikeda, H. Oosato, H. Miyazaki, Y. Sugimoto, “Observation of the enhancement of electric fields normal to the surface using mid-infraed slot antennas and an atomic layer deposition technique,” Opt. Commun., Vol. 349, pp. 98-104, 2015.

[5] T. Wang, P. Li, B. Hauer, D. N. Chigrin, and T. Taubner, “Optical properties of single infrared resonant circular microcavities for surface phonon polaritons,” Nano Lett., Vol. 13, pp. 5051-5055, 2013.

[6] J. Miyata, Y. Yamamoto, Y. Kunichika, T. Kawano, N. Umemori, K. Kasahara, N. Ozaki, N. Ikeda, H. Oosato, and Y. Sugimoto, “Probing enhancement of an electric field perpendicular to an optical antenna surface using SiC surface phonon polaritons,” Proceedings of 10th International Congress on Advanced Electromagnetic Materials in Microwaves and Optics (Metamaterials 2016), Crete, Greece, Poster session II, No. 34, 17-22, Sep. 2016.

D2. Current-Injection Terahertz Lasing in a Distributed-Feedback Dual-Gate Graphene-Channel Transistor

Taiichi Otsuji

Tohoku University

ABSTRACT

This paper reviews recent advancement on the research toward graphene-based terahertz (THz) lasers. Optical and/or injection pumping of graphene can enable negative-dynamic conductivity in the THz spectral range, which may lead to new types of THz lasers. A forward-biased graphene structure with a lateral p-i-n junction was implemented in a distributed-feedback (DFB) dual-gate graphene-channel FET and observed a single mode emission at 5.2 THz at 100K. The observed spectral linewidth fairly agrees with the modal gain analysis based on DFB-Fabry-Perrot hybrid-cavity-mode modeling. Although the results obtained are still preliminary level, the observed emission could be interpreted as THz lasing in population-inverted graphene by carrier-injection.

Keywords: Graphene, terahertz, lasers, current injection, p-i-n junction, transistors

INTRODUCTION

Optical and/or injection pumping of graphene can enable negative-dynamic conductivity in the terahertz (THz) spectral range, which may lead to new types of THz lasers [1],[3]. In the graphene structures with p-i-n junctions, the injected electrons and holes have relatively low energies compared with those in optical pumping, so that the effect of carrier cooling can be rather pronounced, providing a significant advantage of the injection pumping in realization of graphene THz lasers [4],[5]. We implement a forward-biased graphene structure with a lateral p-i-n junction in a distributed-feedback dual-gate graphene-channel field-effect transistor (DFB-DG-GFET) and experimentally observe a single mode emission at 5.2 THz at 100K [7]. The device exhibits a nonlinear threshold-like behavior.

THEORY AND DESIGN

Current injection and population inversion in a dual-gate FET structure

When the intrinsic graphene is optically pumped with the photon energy $\hbar\Omega$, interband transitions lead to the generation of ‘hot’ photoelectron-photohole pairs at energy levels $\hbar\Omega / 2$ above and below the Dirac point, for electrons and holes, respectively [1]-[3]. At room temperature, these photo-excited ‘hot’ electrons and ‘hot’ holes are quasi-equilibrated with the low-energy conduction electrons and valence holes around the Dirac point in the ultrafast time scale of tens of fs due to carrier-carrier scattering, resulting in the quasi-Fermi distribution as shown in Fig. 1 [3]. As a result, quasi-Fermi level of electrons and holes shift *below* and *above* the Dirac point, respectively. At the same time, the high-energy electrons and holes emit optical phonons, losing their energy. Thus the quasi-Fermi distribution, which is originally spreading widely over the energy, shifts closer to the Dirac point, resulting in rapid recovery of the quasi-Fermi level on a ps time scale as shown in Fig. 1 [3],[8]. After the energy relaxation via optical phonon emissions, these non-equilibrium electrons and holes may lose their energies by 'interband' optical phonon scattering, impurity-/disordered scattering, as well as acoustic phonon scattering, or be recombined. Compared to the aforementioned 'intraband' optical phonon scattering, these scattering and recombination processes have longer relaxation times. Therefore the nonequilibrium carriers are piled up around the Dirac point if the pumping intensity is sufficiently high as shown in Fig. 1. This is a situation of carrier population inversion in which the quasi-Fermi level for electrons and holes shifts *above* and *below* the Dirac point, respectively. It is noted that the Auger-type three-particle scattering processes are theoretically forbidden in the ideal graphene [9], but may be dominant in the disordered low-quality graphene and/or under an intense pumping leading to significant many-body effects [10]. The Auger-type scattering lowers the level of population inversion.

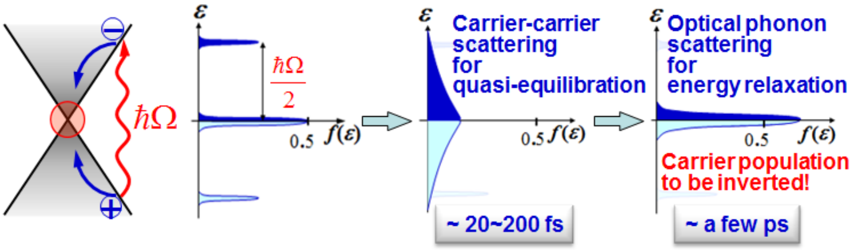

Fig. 1. Nonequilibrium carrier relaxation dynamics in optically pumped intrinsic graphene.

Optical pumping suffers from a significant heating of the electron-hole plasma, which suppresses the population inversion [5],[8]. In the case of the optical pumping with a sufficiently low photon energy, however, the electron-hole plasma can be cooled down [5]. Current injection pumping might allow us to substantially reduce the pumping threshold because the pumping energy could be of the order of "meV" for p-i-n junctions [4]. Figure 2 shows a dual gate p-i-n structure using a graphene-channel field effect transistor (DG-GFET). The gate biasing ($\pm V_g$) controls the injection level, whereas the drain bias (V_{ds}) controls the population inversion. To minimize undesired tunneling current lowering the injection efficiency the distance between the dual gate electrodes must be sufficiently long. The conductivity profiles calculated for typical dimensions and applied bias conditions demonstrate the advantage of current injection for obtaining the THz gain compared to optical pumping [5],[8].

According to Ref. [4], the optical conductivity of graphene channel under the gates and drain biases are estimated as:

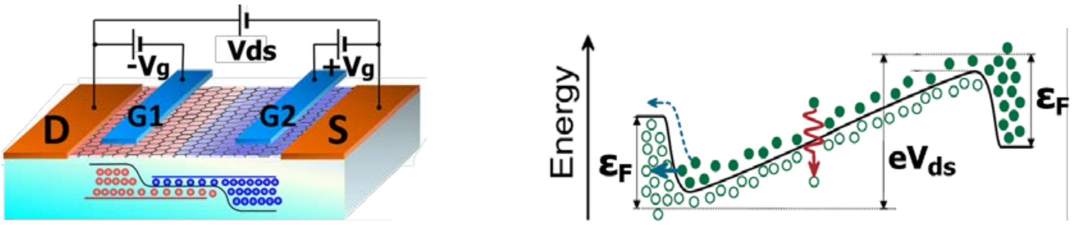

(a) (b)

Fig. 2. Schematic cross-sectional view (a) and corresponding energy band diagram (b) of a lateral p-i-n junction in a DG-GFET for current-injection lasing.

$$\sigma_{\omega} = \sigma_{\omega}^{i\,\mathrm{ntra}} + \sigma_{\omega}^{\mathrm{inter}}, \tag{1}$$

$$\sigma_{\omega}^{\mathrm{intra}} \approx \frac{e^2 \varepsilon_F}{2\pi\hbar^2} \cdot \frac{\tau}{1+\omega^2\tau^2}, \tag{2}$$

$$\sigma_{\omega}^{\mathrm{inter}} \approx \frac{e^2}{2\hbar} \cdot exp\left(\frac{eV - 2e\sqrt{V_F V_g}}{2k_B T}\right) \cdot \sinh\left(\frac{\hbar\omega - eV_{ds}}{2k_B T}\right), \tag{3}$$

where $\sigma_{\omega}^{\mathrm{intra}}$ and $\sigma_{\omega}^{\mathrm{inter}}$ are the intraband and interband component of the conductivity, respectively, e is the elementary charge, ε_F is the Fermi energy reflecting the carrier doping level by applying V_g, $\hbar$ is the reduced Planck constant, τ is the carrier momentum relaxation time, k_B is the Boltzmann constant, and T is the temperature.

Simulated σ_{ω} for typical device geometrical parameters (the gate dielectric thickness of 50 nm , the gate dielectric constant of 4.7, and the carrier momentum relaxation time τ of 2 ps) and various applied voltages V_g and V_{ds} are plotted in Fig. 3. As mentioned above, V_g determines the carrier injection level and corresponding ε_F, whereas V_{ds} determines the level of population inversion (the amount of shifting the quasi-Fermi levels of electrons and holes). When the carrier injection level is relatively low at $V_g = 1.0$ V, a weak V_{ds} produces a net gain (negative conductivity) in a wide THz frequency range. When the carrier injection level increases to $V_g = 10.0$ V, a larger V_{ds} is needed to produce a net gain. The lower cutoff frequency to get the net gain exhibits the blue-shifting For both cases when the V_{ds} increases far above ε_F, the potential slope along the channel becomes manifested resulting in reduction of the carrier injection and corresponding gain (not shown in Fig. 3) [6]. Thus, the lower and upper threshold levels to get the net gain coexist.

Distributed feedback cavity structure

As seen in Fig. 3, the gain medium of graphene itself could not define the transition at single photon energy specifically but exhibits a rather broadband gain spectrum due to the nature of continuum conduction/valence band structures. Thus to obtain a single-mode lasing one needs to install a high-Q laser cavity structure in the dual-gate GFET. In this study, a pair of teeth-brash-shaped gate electrode was patterned to form a distributed feed-back (DFB) cavity in which the active gain area and corresponding gain coefficient are spatially modulated [7],[12] (see Fig. 4(a)). Designed number of the grating periods N, the grating period Λ, the effective refractive index n_{eff}, the Bragg wavelength λ_B, and the principal mode f_P are 16, 12 μm, 2.52, 60.5 μm, and 4.96 THz, respectively. The modal gain of the in-plane waveguided modes in the DFB-DG-GFET was analyzed by taking account of the DFB and the DG-stripline-induced in-plane Fabry-Perot hybridized cavity structures as shown in Fig. 4(b) [7]. One can expect a single-mode lasing at the DFB fundamental mode frequency of 4.96 THz with a spectral Q factor of ~200.

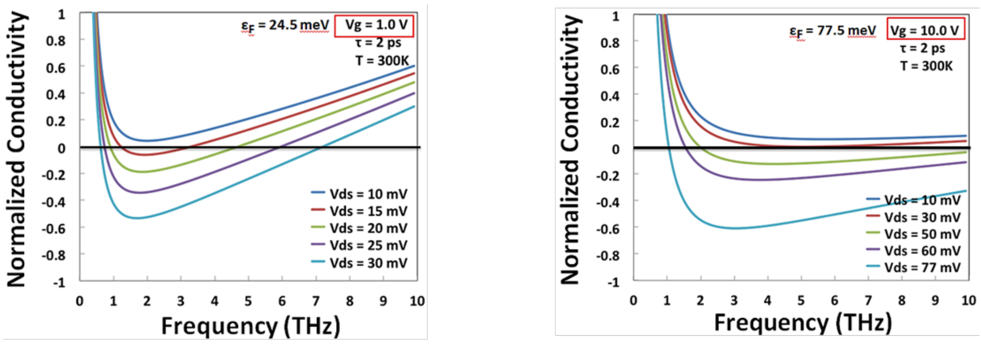

Fig. 3. Simulated optical conductivity for a DG-GFET structure at different V_g and V_{ds} values. The gate dielectric thickness and constant are assumed to be 50 nm and 4.7, respectively.

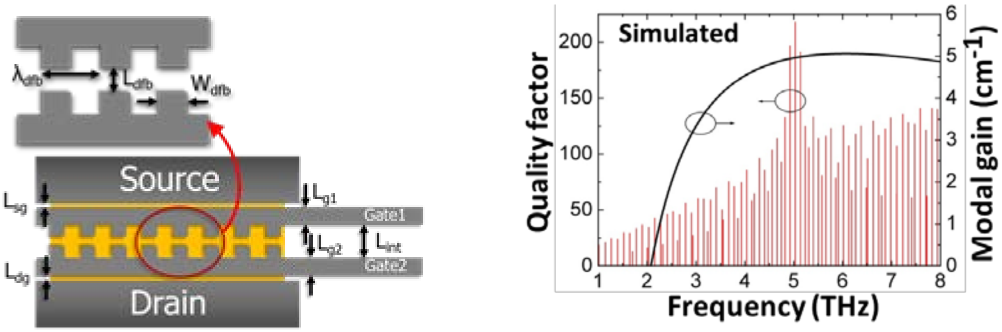

(a) (b)

Fig. 4. (a) The DFB structure and its design parameters in a DFB-DG-GFET. (b) Numerically calculated Q factors and modal gain for in-plane waveguided modes [7].

EXPERIMENTS

Device fabrication

Graphene was synthesized by the thermal decomposition of a C-face 4H-SiC substrate [13]. The Raman spectrum confirmed a high-quality, a few layer non-Bernal stacked graphene (see Fig. 5(a)). The GFET was fabricated using a standard photolithography and a gate stack with a SiN dielectric layer, providing an excellent intrinsic field-effect mobility exceeding 100,000 cm^2/Vs at 300K at the maximal transconductance [14]. A pair of teeth-brash-shaped gate electrode was patterned to form a DFB cavity in which the active gain area and corresponding gain coefficient are spatially modulated (see Figs. 5(b), (c)) [7].

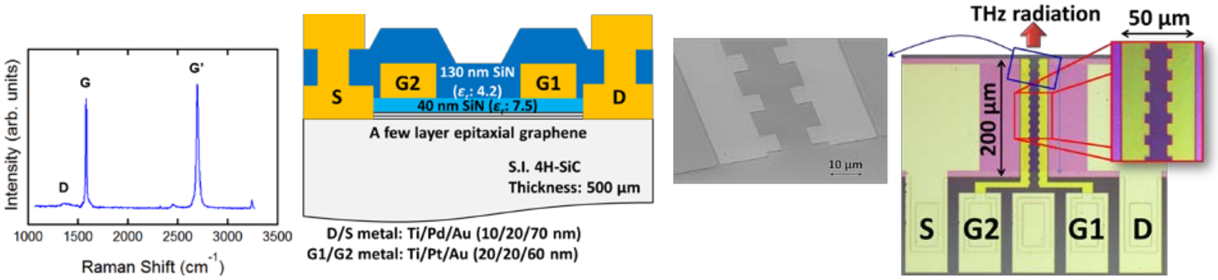

(a) (b) (c)

Fig. 5. (a) Raman spectrum of the epitaxial graphene on 4H-SiC. (b) Device cross-section. (c) Device SEM and photo images [7].

The device exhibited ambipolar behaviors on its current-to-gate-voltages (V_{g1}, V_{g2}) characteristics as shown in Fig. 6 [7]. With a complimentary biased V_{g1} and V_{g2} with a positive drain-source bias V_{ds} the carrier population can be inverted [4].

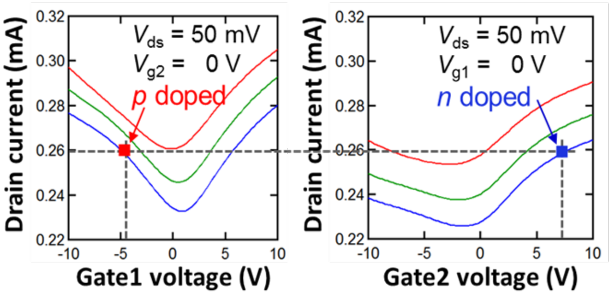

Fig. 6. Measured ambipolar current-voltage characteristics for a fabricated DFB-DG-GFET [7].

THz emission characteristics [7]

THz emission from the sample was measured at 300 and 100K using a Fourier-transform spectrometer with a 4.2K-cooled Si bolometer. The background blackbody radiation was first observed under the zero-bias condition, which was subtracted from the one observed under biased conditions. The observed spectra contain huge systematic noise at around 3.6-4.2 THz due to misalignment of the Martin-Puplett interferometer so that it was disregarded (see Fig. 7(a)). No distinctive emission at 300 K, but rather sharp single mode emission at 5.2 THz was observed at 100K (see Figs. 7(a), (b)) when V_{ds} is positively applied to a certain level under symmetric electron and hole injection conditions. The single mode emission exhibits a non-monotonic threshold-like behavior as shown in Fig. 8 with the highest intensity ~10 µW. This peculiar phenomena might reflect the carrier over-cooling effect under weak pumping [5]. Spectral narrowing with increasing the carrier injection around the threshold was also observed. The emission spectra at V_{ds} = 0.5 V can fit to the Lorentzian curve with a Q factor of 170 (a linewidth of 30.6 GHz), which fairly agrees with the simulated results shown in Fig. 4(b).

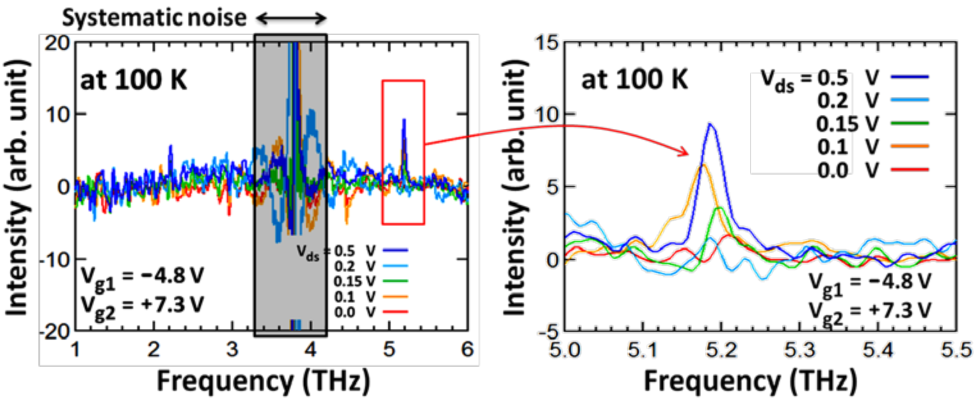

Fig. 7. Observed emission spectra at 100K (a) in a broad range and (b) in a magnified range at around 5.2 THz [7].

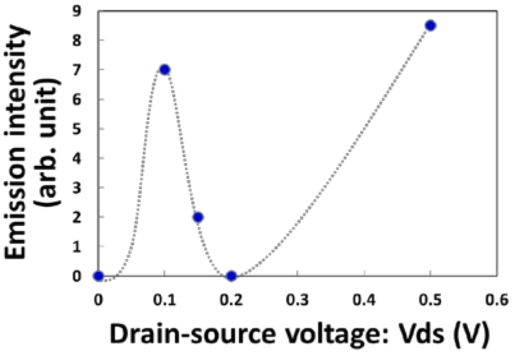

Fig. 8. Nonlinear threshold-like behavior of the THz emission intensity vs. V_{ds} [7].

Discussion

The conductivity analysis shown with Eqs. (1)-(3) suggests that much higher Q factors and/or higher quality of graphene material having longer momentum relaxation times are/is needed to enable the single-mode intense lasing at room temperature. The Q factors of the DFB structure can be further increased by orders by increasing the number of the DFB periods as well as by introducing a thick dielectric layer on top of the device to maximize the spontaneously-emitted THz photon field at the graphene channel area. These are future subjects.

CONCLUSION

A forward-biased graphene structure with lateral p-i-n junctions was implemented in a DFB-DG-GFET and experimentally observed a single mode emission at 5.2 THz at 100K. The device exhibited a nonlinear threshold-like behavior with respect to the current-injection level. The observed spectral linewidth fairly agrees with the modal gain analysis based on DFB-Fabry-Perot hybrid-mode modeling. Although the results obtained are still preliminary level, the observed emission could be interpreted as THz lasing in population-inverted graphene by carrier-injection.

ACKNOWLEDGEMENTS

The author thanks V. Ya. Aleshkin, H. Wako, D. Yadav, H. Fukidome, M. Suemitsu, E. Sano, V. Mitin, and M.S. Shur for their contributions. We also thank T. Palacios and Q. Hu for valuable discussions. This work was financially supported in part by JSPS-KAKENHI (No. 23000008 and 16H06361), Japan. The work by A.D. was supported by the Dynasty Foundation, Russia. The DFB-DG-GFET process was done at the Nano-Spin facility, RIEC, Tohoku University, Japan.

References

[1] Ryzhii, V., Ryzhii, M., Otsuji, T., "Negative dynamic conductivity in optically pumped graphene," *J. Appl. Phys.* **101**, 083114-1-4, 2007.

[2] Otsuji, T., Boubanga-Tombet, S., Satou, A., Ryzhii, M. and Ryzhii, V., "Terahertz-wave generation using graphene-toward new types of terahertz lasers," *IEEE J. Selected Topics in Quantum Electron.* **19**, 8400209-1-9, 2013.

[3] Otsuji, T., Boubanga Tombet, S. A., Satou, A., Fukidome, H., Suemitsu, M., Sano, E., Popov, V., Ryzhii, M., and Ryzhii, V., "Graphene-based devices in terahertz science and technology," *J. Phys. D: Appl. Phys.* **45**, 303001-1-9, 2012.

[4] Ryzhii, M. and Ryzhii, V., "Injection and population inversion in electrically induced p-n junction in graphene with split gates," *Jpn. J. Appl. Phys. (L)* **46**, 151-153, 2007.

[5] Ryzhii, V., Ryzhii, M., Mitin, V. and Otsuji, T., "Toward the creation of terahertz graphene injection laser," *J. Appl. Phys.* **110**, 094503-1-9, 2011.

[6] Ryzhii, V., Semenikhin, I., Ryzhii, M., Svintsov, D., Vyurkov, V., Satou, A., and Otsuji, T., "Double injection in graphene p-i-n structures," *J. Appl. Phys*. **113**, 244505-1-9, 2013.

[7] Tamamushi, G., Watanabe, T., Dubinov, A.A., Mitsushio, J., Wako, H., Satou, A., Suemitsu, T., Fukidome, H., Suemitsu, M., Ryzhii, M., Ryzhii, V., and Otsuji, T., "Single-mode terahertz emission from current-injection graphene-channel transistor under population inversion," the 74th Dev. Res. Conf. Dig., **1**, 225-226, 2016.

[8] Satou, A., Ryzhii, V., Kurita, Y., and Otsuji, T., "Threshold of terahertz population inversion and negative dynamic conductivity in graphene under pulse photoexcitation," *J. Appl. Phys.* **113**, 143108, 2013.

[9] Foster, M.S., and Aleiner, I.L., "Slow imbalance relaxation and thermoelectric transport in graphene," *Phys. Rev. B* **79**, 085415-1-14, 2009.

[10] Winzer, T., and Malic, E., "Impact of Auger processes on carrier dynamics in graphene," *Phys. Rev. B* **85**, 241404(R)-1-5, 2012.

[11] Tani, S., Blanchard, F., and Tanaka, K., "Ultrafast carrier dynamics in graphene under a high electric field," *Phys. Rev. Lett.* **99**, 166603-1-5, 2012.

[12] Williams, W.S., Kumar, S., and Hu, Q., “Distributed-feedback terahertz quantum-cascade lasers with laterally corrugated metal wavuguides,” *Opt. Lett.* **30**, 2909-11, 2005.

[13] Fukidome, H., Kawai, Y., Fromm, F., Kotsugi, M., Handa, H., Ide, T., Ohkouchi, T., Miyashita, H., Enta, Y., Kinoshita, T., Seyller, T., and Suemitsu, M., “Precise control of epitaxy of graphene by microfabricating SiC substrate,” *Appl. Phys. Lett.* **101**, 041605, 2012.

[14] Satou, A., Tamamushi, G., Sugawara, K., Mitsushio, J., Ryzhii, V., and Otsuji, T., “A fitting model for asymmetric I-V characteristics of graphene field-effect transistors for extraction of intrinsic moblities,” *IEEE Trans. Electron Dev.*, **63**, 3300-3306, 2016.

D3. Terahertz Photonic Crystals

Masayuki Fujita
Osaka University

Terahertz (THz) electromagnetic waves, which are located in the frequency region between radio and infrared light waves from 0.1 THz to 10 THz, have attracted considerable interest in the interdisciplinary fields of photonics and electronics [1]. Currently, their unique potential applications such as in spectroscopic sensing, nondestructive imaging, and broadband wireless communication, are being developing. However, most existing THz application systems are composed of bulky and discrete components. Consequently, the exploration of techniques to control THz waves in a thin, planar, and low-loss structure is indispensable toward the practical use of the THz technology in various fields.

Photonic crystals, composed of a dielectric material with a periodic refractive-index distribution on a scale comparable to the wavelengths of interest, are analogous to solid-state crystals with periodic potential distributions. The photonic crystal can create an exotic dispersion relationship between the frequency and wave vectors to enable the manipulation of photons or electromagnetic waves. Appropriate photonic-crystal designs show a photonic bandgap (PBG) where no optical modes exist. Introducing an artificial defect into the photonic crystal by disturbing the periodicity can enable the development of compact and low-loss photonic components in the PBG region. The propagation of light can be changed according to the dispersion properties of a photonic crystal. At the photonic-band edge, the group velocity approaches zero. The slow light or the standing-wave condition is thus formed by the distributed-feedback effect to enhance the interaction between the light and matter, causing resonance. Two-dimensional (2D) photonic-crystal slabs, which have a 2D periodic lattice of air holes on a semiconductor slab, are promising for practical applications owing to their simple planar structures.

Recently, the 2D photonic-crystal slab was studied as a platform for THz-wave manipulation with sufficient confinement and efficient interaction [2–5]. Silicon photonic-crystal slabs are especially promising because they can be easily fabricated with great accuracy using well-established semiconductor micromachining techniques, and the absorption loss because of free carriers can be managed by varying the carrier density or resistivity.

A compact THz waveguide in the PBG region can be created by introducing a line defect in the photonic crystal that disturbs the periodicity [6]. No radiation loss is theoretically predicted because the THz waves are completely confined in both the vertical and in-plane directions by total internal reflection and the PBG effect, respectively. To measure the propagation loss in the 0.3-THz band, photonic-crystal waveguides with a period of 240 μm and various propagation lengths were fabricated using a 200-μm-thick silicon substrate with a resistivity of ~20 kΩ·cm. The transmission loss of the waveguides was measured using a THz spectroscopic system based on continuous-wave tunable electronic sources employing a WR-3 hollow waveguide. To efficiently couple the WR-3 and photonic-crystal waveguides, tapered structures were created at the end of the photonic-crystal waveguides. When the tapered structure is directly plugged into the WR-3 waveguide, an extremely small insertion loss (lower than 0.2 dB) is achieved, because the adiabatic change in the refractive index of the tapered structure reduces the reflection. The measured propagation loss was less than 0.1 dB/cm in the frequency range of 0.326–0.331 THz, and the minimum loss was 0.04 dB/cm at 0.330 THz. This value is two or three orders of magnitude smaller than that reported for metallic lines in the 0.3-THz band. In addition, this value is the smallest ever reported for various photonic-crystal waveguides, including those in the light-wave region. This indicates that the propagation loss in photonic-crystal waveguides in the THz region is not determined by radiation loss arising from structural errors, as reported for the light-wave region, but by material absorption.

The ultralow-loss photonic-crystal waveguide technique demonstrated here is applicable to various compact and low-loss THz components such as cavities, filters, diplexers, bends, branches, and couplers, may potentially lead to the development of THz integrated circuits based on a photonic-crystal slab.

In the microcavity based on the photonic-crystal slab, *Q* factors over 9,000 in a cavity formed by a line defect of three missing holes in a triangular-lattice pattern of air holes were reported for the 0.3-THz band [7]. Such microcavities may be applicable to highly sensitive THz wave sensing systems for advanced spectroscopic applications.

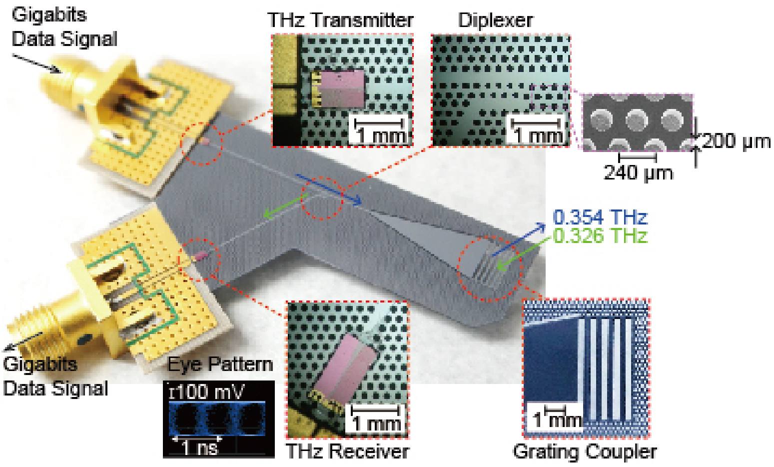

Fig. 1. Prototype of THz transceiver using a photonic-crystal platform

A compact THz diplexer (frequency selector) was designed using a silicon photonic-crystal directional coupler of length comparable to the operation wavelength [8, 9]. The operation was demonstrated with the bandwidth of 2% and a 40-dB isolation between two input ports. Based on the photonic-crystal diplexer, a THz transceiver for wireless communications employing frequency-division multiplexing was developed [10], as shown in Fig. 1. A grating coupler was used for an input-output wireless interface for free-space communication. Resonant tunneling diodes (RTDs) were used as THz receivers and transmitters, and were mounted on a photonic-crystal waveguide [11, 12]. Wireless transmission experiments of the transceiver were performed using an electric transmitter and receiver based on a WR-3 horn antenna and hollow waveguide. The opened eye diagrams at 1.5 Gbit/s and an oscillation spectrum were successfully observed at the RTD receiver (0.326 THz) and transmitter (0.354 THz), respectively. However, the measured bit-error rate was limited to 5×10^{-4} due to low signal power. The most important factor in improving the signal power is the enhancement of the coupling efficiency between the RTD and photonic-crystal waveguide.

A photonic crystal exhibits not only the PBG effect but also the photonic band-edge effect due to the dispersion relation. For the band-edge condition where the period matches the wavelength in the medium, the electromagnetic waves propagating in various directions are combined by Bragg reflection to form a standing wave. Simultaneously, the diffraction condition of the wave is satisfied in the direction normal to the photonic-crystal plane, because the Bragg condition is also satisfied in that direction. This phenomenon can be utilized for the trapping of a THz wave in a photonic-crystal slab [13], as shown in Fig. 2. An incident THz wave is trapped in the photonic-crystal slab, and an in-plane resonant mode is excited. When the material of the slab shows no absorption, the trapped wave is eventually released from the slab and observed from outside with a low damping decay. On the other hand, the introduction of appropriate free carriers in the slab by exciting or doping the material allows the trapped THz wave to be efficiently captured within the slab by absorption, despite its structure being thinner than the wavelength of the THz wave. Thus, the trapped THz wave can be controlled by changing the density of free carriers through the change in pumping condition or the resistivity of the material.

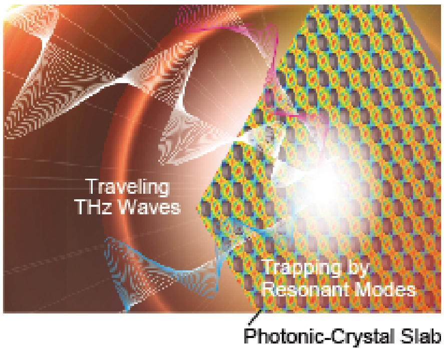

Fig. 2. Image of THz-wave trapping in a photonic-crystal slab

To investigate the dynamics of the THz-wave trapping and capture process for the 0.3-THz band, a silicon photonic-crystal slab with a square lattice of air holes was employed. The temporal response of the transmission wave was measured by using an optical-pump/THz-probe system [3]. The spectrogram for the sample without pumping shows that the components trapped by the photonic crystal are slowly released from the slab at a resonant frequency of ~0.3 THz. On the other hand, when the photonic crystal was pumped with a 775-nm laser light synchronized with the THz wave, the transmission signal was dramatically reduced owing to the effective interaction between the trapped THz wave and the material absorption by excited free carriers.

To demonstrate the application of the THz-wave dynamic control in a photonic-crystal slab, on-off modulation experiments of THz wireless transmission were performed [3]. A continuous THz wave was introduced into a photonic-crystal slab and was modulated by the photoexcitation with a 775-nm laser modulated by a pulse-pattern generator. The signal received through the photonic crystal was detected by a Schottky barrier diode module and the received signal was analyzed using an oscilloscope. A signal was observed when the pumping laser was off, while no signal was detected for the pump-on condition, owing to the capture of the THz wave in the photonic crystal. This result successfully demonstrates the modulation of a THz wave in a photonic crystal. The modulation speed was limited to below 1 MHz owing to the long carrier lifetime in silicon. The reduction in the carrier lifetime would enable a faster modulation (beyond 10 GHz) by the introduction of ion implantation, a carrier removal structure such as a PIN diode, or the use of other materials with faster carrier lifetimes, such as a low-temperature-grown GaAs or graphene.

As an application of the capture of THz wave in a photonic-crystal slab, broadband absorbers, which are crucial components for stabilizing THz systems by reducing multiple reflection and interferences, were developed [13, 14]. The THz-wave absorber was composed of a photonic-crystal slab and a reflection mirror. The broadband operation was realized by using triple-band resonance involving three types of resonances—even and odd modes of the in-plane resonance, and Fabry-Pérot resonance between the photonic-crystal slab and the mirror. By superposing the absorption peaks originating from these resonant modes, a flat-top broadband absorption spectrum can be achieved. To achieve high absorptivity, the resistivity of silicon was optimized to be ~6 Ω·cm to satisfy the matching condition. A measured peak absorptivity was over 99 % at 0.3 THz and the bandwidth (absorptivity ≥ 90%) was as broad as 17 % of the operation frequency. This performance was achieved despite the simplicity of the structure, with an overall thickness of approximately half a wavelength. This absorber was applied to a THz proximity wireless communication system to suppress the standing wave effect between the transmitter and receiver. The photonic-crystal absorber successfully stabilized the communication system by reducing multiple reflections.

In addition, preliminary results on THz sensing application using the THz-wave trapping of a photonic-crystal slab were reported by the sensing of a single-layer graphene [4].

In conclusion, a photonic crystal is a potential candidate to form a core technology platform for various THz devices and components. The results will prospectively lead to the realization of THz integrated circuits that reduce the size of THz systems for use in advanced THz applications, including information and communication technology, spectroscopic sensing, and nondestructive imaging. Based on the successful achievements, the CREST research project entitled “Development of terahertz integrated technology platform through fusion of resonant tunneling diodes and photonic crystals” funded by Japan Science and Technology Agency from 2015 was started in Japan.

References

[1] T. Nagatsuma, S. Hisatake, M. Fujita, H. H. N. Pham, K. Tsuruda, S. Kuwano, and J. Terada, “Millimeter-wave and terahertz-wave applications enabled by photonics,” *IEEE J. Quantum Electron.*, vol. 52, no. 1, pp. 0600912-1– 0600912-12, 2016.

[2] M. Fujita, K. Tsuruda, A. Suminokura, M. Yata and T. Nagatsuma, “Silicon photonic crystal as a terahertz-wave technology platform,” *The 4th International Symposium on Photonics and Electronics Convergence*, no. E-3, 2014.

[3] M. Fujita, “Photonic-crystal slab for terahertz-wave technology platform,” *Proc. SPIE*, vol. 9757, pp. 97570W-1–97570W-8, 2016.

[4] M. Fujita, “Terahertz-wave manipulation using photonic-crystal slabs and its applications,” OYO BUTURI, vol. 85, no.6, pp. 490–495, 2016.

[5] M. Fujita, “Terahertz photonic crystals and their applications,” *The 12th International Symposium on Photonic and Electromagnetic Crystal structures*, 2016.

[6] K. Tsuruda, M. Fujita, and T. Nagatsuma, “Extremely low-loss terahertz waveguide based on silicon photonic-crystal slab,” *Opt. Express*, vol. 23, no. 25, pp. 31977–31990, 2015.

[7] K. Tsuruda, K. Okamoto, S. Diebold, S. Hisatake, M. Fujita, and T. Nagatsuma, “Terahertz sensing based on photonic crystal cavity and resonant tunneling diode,” *Proc. PIERS*, pp. 3922–3926, 2016.

[8] M. Yata, M. Fujita and T. Nagatsuma, “Diplexer for terahertz-wave integrated circuits using a photonic-crystal slab,” *International Topical Meeting on Microwave Photonics / The 9th Asia-Pacific Microwave Photonics Conference*, no. Tu-C3, pp. 40–43, 2014.

[9] M. Yata, M. Fujita, and T. Nagatsuma, “Photonic-crystal diplexers for terahertz-wave applications,” *Opt. Express*, vol. 24, no. 7, pp. 7835–7849, 2016.

[10] M. Fujita and T. Nagastuma “Photonic crystal technology for terahertz system integration,” *Proc. SPIE*, vol. 9856-21, pp. 98560O-1–98560O-10, 2016.

[11] A. Suminokura, K. Tsuruda, T. Mukai, M. Fujita and T. Nagatsuma, “Integration of resonant tunneling diode with terahertz photonic-crystal waveguide and its application to gigabit terahertz-wave communications,” *International Topical Meeting on Microwave Photonics / The 9th Asia-Pacific Microwave Photonics Conference*, no. ThB-3, pp. 419–422, 2014.

[12] K. Tsuruda, M. Fujita, A. Suminokura, M. Yata and T. Nagatsuma, “Terahertz-wave integrated circuits based on photonic crystals,” *Proc. PIERS*, pp. 2254–2259, 2015.

[13] R. Kakimi, M. Fujita, M. Nagai, M. Ashida and T. Nagatsuma, “A photonic-crystal terahertz-wave absorber and its application to terahertz communications,” *The 4th International Symposium Terahertz NanoScience*, 2014.

[14] R. Kakimi, M. Fujita, M. Nagai, M. Ashida and T. Nagatsuma, “Capture of a terahertz wave in a photonic-crystal slab,” *Nature Photon.*, vol. 8, no. 8, pp. 657–663, 2014.

D4. THz-Wave Emitters and Detectors Based on Diode Technology

Hiroshi Ito
Kitasato University

1. Introduction

Terahertz (THz) wave emitters and detectors are the key components for constructing various THz wave systems. In particular, semiconductor-based diodes are important because they have good reliability and reasonable cost and because they are suitable for integration with other components. This report describes two types of diode-based devices. One is a THz wave emitter (photomixer) consisting of a uni-traveling-carrier photodiode (UTC-PD), and the other is a THz wave detector (rectifier) consisting of a Schottky barrier diode (SBD) or a Fermi-level managed barrier (EMB) diode.

2. THz-wave emitter

The photomixer is a promising device for generating continuous THz waves because it has several important features, such as wide frequency tunability, good frequency stability, narrow line width, and the capability for long distance transmission of high frequency signals through low loss fibers. The basic requirements for the photomixer are for them to have both high operation speed and large output current. In these regards, the UTC-PD is one of the best solutions because it provides both a high 3-dB down bandwidth and a high saturation output current. To transmit high frequency electromagnetic waves in a wide frequency range, the photomixer needs to be integrated with a planar antenna, and there are two choices for this. One is a broadband antenna with constant characteristic impedance regardless of the operation frequency, and the other is a resonant antenna for increasing the radiation efficiency at around the designated frequency while moderately reducing its operational bandwidth.

2.1 Broadband-antenna integrated UTC-PD

Self-complementary antennas, such as log-periodic antennas, log-spiral antennas, and 90º bowtie antennas, are frequently used as broadband antennas. However, we have to be careful in using these antennas because the polarization of the emitted signal from them sometimes strongly depends on the operation frequency. Figure 1 shows the dependence on frequency of the relative principal polarization axis angle (polarization angle) for the emitted signals from a log-periodic-antenna integrated UTC-PD and a 90º bowtie-antenna integrated UTC-PD [1]. The behaviors are quite different. The polarization angle of the log-periodic antenna device drastically changes with frequency, while that of the bowtie antenna device remains almost the same. These differences come from the difference in the antenna electrode pattern, and the reflection symmetry in the antenna pattern is essential for stable and linear polarization characteristics [1, 2]. The precise control of the polarization characteristics is especially important for applications that require polarization discrimination, such as radar, wireless communication, ellipsometry [3, 4], imaging, and spectroscopy.

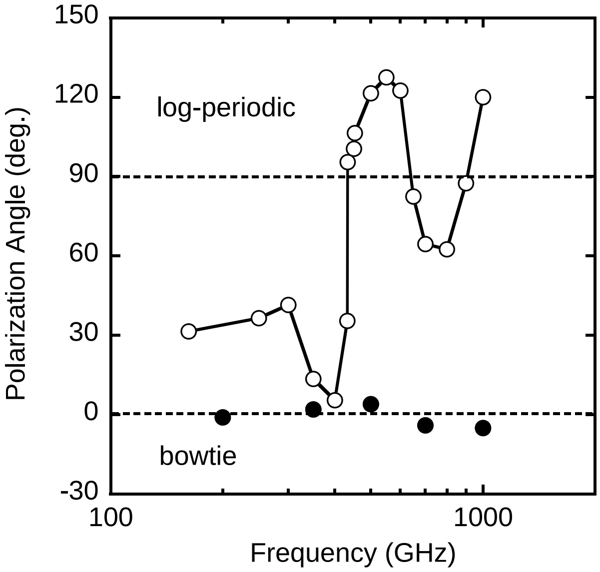

Fig. 1. Dependence on frequency of relative principal polarization axis angle for emitted signals from a log-periodic-antenna integrated UTC-PD and a bowtie-antenna integrated UTC-PD.

Another important consideration for the UTC-PD to enable operations at very high-frequencies is the carrier transport in the device. We performed both analytical calculations and experimental characterization on the high frequency characteristics of the UTC-PD photomixers, showing that locating its absorber on the anode side is generally required to extend the 3-dB down bandwidth of a UTC-PD [5]. The optimized absorber design is obtained using a certain partition of absorber thickness into p-type and depleted absorbers, depending on the total absorber thickness. A comparison of the observed dependence on frequency of the output power in a UTC-PD with calculated ones showed that the effective electron velocity can be as high as 6×10^7 cm/s in the depletion layer [5]. This behavior results from the electron velocity overshoot effect that is sensitive to the field intensity. Benefitting from such superior carrier transport, THz-wave emissions from a UTC-PD at frequencies of up to 3 THz were accomplished [6].

2.2 Resonant-antenna integrated UTC-PD

We investigated two types of antennas as resonant antennas, a slot antenna and a resonant bowtie antenna, for integration with a UTC-PD. The former is effective for obtaining both an increased output power and a relatively wide bandwidth, and the latter can be designed using a simple analytical calculation based on a discrete circuit model including transmission lines.

Figure 2 shows the dependence on frequency of the output power generated from the fabricated slot-antenna-integrated UTC-PD modules [6, 7]. The output power from the broadband bowtie-antenna-integrated device is also plotted for comparison. The output power from the slot-antenna-integrated UTC-PDs was obviously larger than that from the bowtie-antenna-integrated UTC-PD in a frequency range from about 900 GHz to 1.6 THz for the slot-A (narrow-slot) device and from 350 to 850 GHz for the slot-B (wide-slot) device. These relatively wide bandwidths are due to the relatively weak resonance of the integrated slot antennas. The maximum output power enhancement ratios were found to be about 2.3 at around 1.25 THz for the slot-A device and about 3.3 at around 650 GHz for the slot-B device.

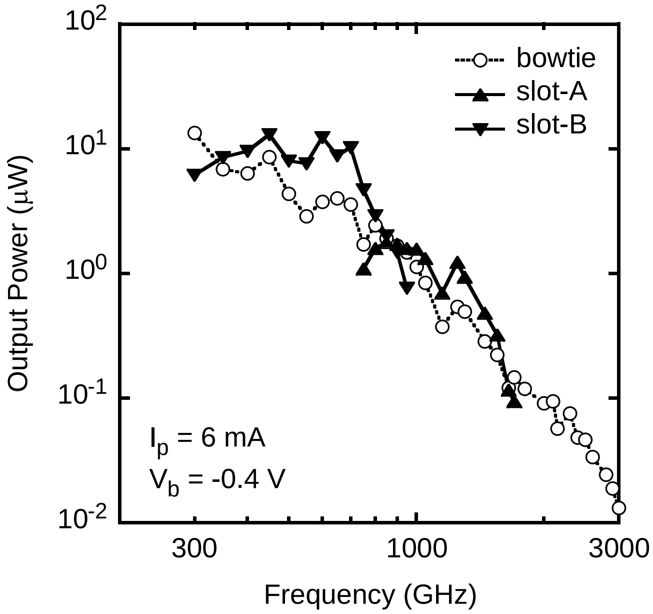

Fig. 2. Dependences on frequency of output power generated from slot-antenna-integrated UTC-PD. The output power from the bowtie-antenna-integrated UTC-PD is also plotted for comparison.

Another candidate is a resonant bowtie antenna with two connecting electrodes on both sides of the UTC-PD [8], which can be designed using an analytical calculation without using an electro-magnetic simulator. The output power was enhanced at frequencies from about 400 to 700 GHz and the peak enhancement ratio was about three at 550 GHz. These behaviors are fairly consistent with the analytical calculation, indicating that the resonant-bowtie antenna can be accurately designed without the electro-magnetic simulation.

3. THz-wave detectors

A rectifier-based THz-wave detector has been widely used in numerous applications. A typical one is the SBD. We investigated an InP-based SBD because it is suitable for zero-biased operation and integration with other InP-based high-speed electron and photonic devices. Another topic is the development of a new type of THz-wave detector named a Fermi-level managed barrier (FMB) diode.

3.1 Schottky barrier diode

Similar to the emitter, the polarization characteristics of the detector are also important for several applications, and they strongly depend on the antenna design. We fabricated an extended-bowtie-antenna-integrated InGaAsP SBD [9] and accomplished a stable polarization angle within ±1.5° at frequencies from 80 to 600 GHz. The degree of polarization was larger than 95% within this frequency range and more than 97.5% below 400 GHz. The extinction ratio was less than 2.6% up to 600 GHz and less than 1.2% below 400 GHz. These results indicate that the fabricated SBD module has adequate linearly polarized detection characteristics in the sub-THz-wave range. The polarization controlled UTC-PD [1] and the SBD [9] were successfully applied to the millimeter-wave ellipsometry without utilizing an external polarizer [2].

3.2 Fermi-level managed barrier diode

Although the SBD is an excellent THz-wave detector, its characteristics may still need to be improved. Because the Schottky barrier height is largely influenced by less-controllable surface states in semiconductors, its characteristics are sometimes unstable and irreproducible. In addition, the rather large differential resistance of the small-sized SBD is also a concern in terms of the impedance matching among the input antenna, detector diode, and read-out circuit. The large resistance of the SBD also results in large thermal noise, which will cause increased noise equivalent power (NEP) in THz-wave detection. To improve these points, we developed a novel InP/InGaAs hetero-barrier rectifier named an FMB diode [10-14]. The primary feature of the FMB diode is that it can easily achieve a very low barrier height, which is effective for decreasing diode resistance, increasing output current, and attaining both low-noise detection and broadband operation. In addition, because it consists entirely of semiconductor layers, its characteristics are stable, controllable, and reproducible.

Figure 3 shows a schematic band diagram of the FMB diode. The Fermi-level in heavily doped n-InGaAs is located above the conduction band edge depending on the carrier density, which is called the “band-filling effect.” By using this phenomenon, we can control the barrier height at the InP/InGaAs hetero-interface from zero to a value for the conduction-band discontinuity and can make the barrier height (differential resistance) of the diode very small [10-14].

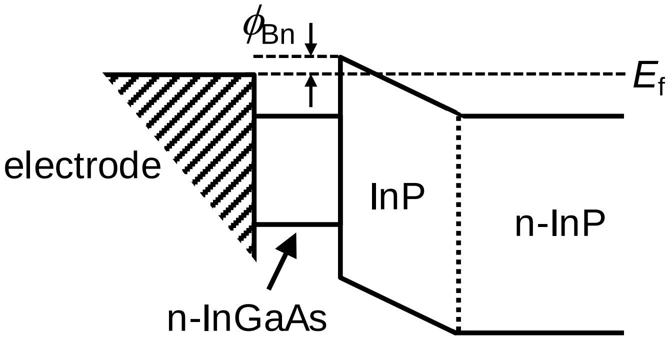

Fig. 3. Schematic band diagram of Fermi-level managed barrier (FMB) diode.

An antenna-integrated InP/InGaAs FMB diode was fabricated and assembled in a quasi-optical package with a pre-amplifier. Figure 4 shows the measured voltage sensitivity of the fabricated FMB diode module against frequency [13, 14]. We confirmed signal detection at frequencies from 160 GHz to 1.4 THz with the fabricated module. The peak voltage sensitivity obtained was as high as 3.2 MV/W at 300 GHz, and the sensitivity at 1 THz was still considerably high at about 290 kV/W. We also evaluated the NEP of the FMB diode module and obtained values as small as 3.0 pW/Hz$^{0.5}$ at 300 GHz and 33 pW/Hz$^{0.5}$ at 1 THz. These values are considerably lower than those for commercially available zero-biased broadband SBD detectors, demonstrating that the FMB diode is a promising solution for broadband and low noise THz-wave detection.

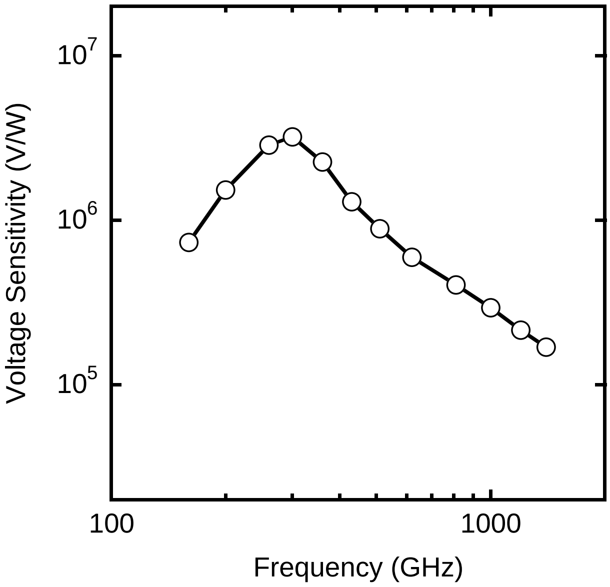

Fig. 4. Dependence on frequency of voltage sensitivity for preamplifier-integrated FMB diode module.

4. Conclusion

Developments in diode-based THz wave emitters and detectors were described. A photomixer-based THz wave emitter consisting of an antenna-integrated UTC-PD demonstrated a polarization-controlled output signal up to 3 THz. A resonant antenna was also effective for increasing the output power from a UTC-PD while maintaining a relatively wide bandwidth. A rectifier-based THz wave detector consisting of the SBD also demonstrated polarization-controlled detection characteristics. A new type of THz-wave detector named an FMB diode was also developed, and it demonstrated a broad operational bandwidth and a very low NEP of 3.0 pW/Hz$^{0.5}$ at 300 GHz.

References

[1] H. Ito, T. Yoshimatsu, H. Yamamoto, and T. Ishibashi, “Photonic Terahertz-Wave Emitter Integrating Uni-Traveling-Carrier Photodiode and Self-Complementary Planar Antenna,” Optical Engineering, Vol. 53, No. 3, pp. 031209-1 - 031209-7, 2014.

[2] H. Ito, T. Yoshimatsu, H. Yamamoto, and T. Ishibashi, “Widely Tunable THz-Wave Emitter with Linear Polarization Characteristics Based on Antenna-Integrated UTC-PD,” Proc. SPIE, Vol. 9199, pp. 919908-1 - 919908-8, 2014.

[3] H. Yamamoto and H. Ito, “Millimeter-Wave Ellipsometry Using Low-Coherence Light Source,” IEICE Trans. Electron., Vol. E97-C, No. 5, pp. 460-462, 2014.

[4] H. Yamamoto and H. Ito, “Millimeter-Wave Ellipsometry Using Interface-Planarization Prism,” IEICE Trans. Electron., Vol. E98-C, No. 8, pp. 873-877, 2015.

[5] T. Ishibashi, Y. Muramoto, T. Yoshimatsu, and H. Ito, “Uni-Traveling-Carrier Photodiodes for Terahertz Applications,” IEEE J. Selected Topics in Quantum Electronics, Vol. 20, No. 6, pp. 3804210-1 - 3804210-10, 2014.

[6] H. Ito, T. Yoshimatsu, H. Yamamoto, and T. Ishibashi, “Enhanced-Output-Power Broadband Terahertz-Wave Emitter Based on Slot-Antenna-Integrated Uni-Travelling-Carrier Photodiode,” Electron. Lett., Vol. 51, No. 21, pp. 1670-1671, 2015.

[7] H. Ito, T. Yoshimatsu, H. Yamamoto, and T. Ishibashi, “Enhancement of THz-Wave Output Power Using Slot-Antenna-Integrated Uni-Traveling-Carrier Photodiode,” Proc. SPIE, Vol. 9585, pp. 958506-1 - 958506-7, 2015.

[8] T. Ishibashi, Y. Muramoto, T. Yoshimatsu, and H. Ito,” Generation and Detection of Continuous THz-wave Radiation by Diode Technologies,” 2015 IEEE Photonics Conference (IPC) Proc., pp. 116-117, 2015.

[9] H. Ito, “Broadband Terahertz-Wave Detector Implementing Zero-Biased InGaAsP Schottky-Barrier Diode,” Proc. SPIE, Vol. 9483, pp. 948307-1 - 948307-9, 2015.

[10] H. Ito and T. Ishibashi, “Fermi-Level Managed Barrier Diode for Broadband and Low-Noise Terahertz-Wave Detection,” Electron. Lett., Vol. 51, No. 18, pp. 1440-1442, 2015.

[11] H. Ito and T. Ishibashi, Novel Fermi-Level Managed Barrier Diode for Broadband and Sensitive Terahertz-Wave Detection,” Proc. International Conference on Infrared, Millimeter, and Terahertz Waves (IRMMW-THz 2015), pp. W1D3-1 - D1D3-2, 3133416-1 - 3133416-2, 2015.

[12] H. Ito and T. Ishibashi, “Broadband and High-Sensitivity Terahertz-Wave Detection Using Fermi-Level Managed Barrier Diode,” Proc. SPIE, Vol. 9856, pp. 985624-1 - 985624-8, 2016.

[13] H. Ito and T. Ishibashi, “Low Noise Terahertz-Wave Detection by InP/InGaAs Fermi-Level Managed Barrier Diode,” Appl. Phys. Express, Vol. 9, No. 9, pp. 092401-1 - 092401-3, 2016.

[14] H. Ito and T. Ishibashi, “Broadband and Low NEP Terahertz-Wave Detection Using Preamplifier-Integrated Fermi-Level Managed Barrier Diode,” Proc. International Conference on Infrared, Millimeter, and Terahertz Waves (IRMMW-THz 2016), pp. H4C.3-1-1 - H4C.3-2, 2016.

D.5 Millimeter-wave and submillimeter-wave antennas in standard CMOS technology

Eiichi Sano

Hokkaido University

The crowded bands of 2.4 and 5 GHz will push the operation bands of wireless communication systems to the millimeter (MM)-wave region (e.g., 60 GHz). Reduced sizes of antennas in the MM-wave region enable them to be monolithically integrated with CMOS RF and baseband circuits. Furthermore, on-chip antennas in standard CMOS processes can contribute to reducing costs. However, low-resistivity (~10 Ω-cm) Si substrates commonly used in standard CMOS technology degrade the antenna gain. Figure 1 summarizes the antenna gain versus frequency characteristics reported in the literature [1–19]. The antenna gains on low-resistivity substrates remain ~10 dB lower than those on high-resistivity substrates. Thus, an ingenious development is needed to increase the gains of antennas fabricated on low-resistivity Si substrates. Since Pendry's claim that materials with a negative refractive index can act as perfect lenses [20], metamaterials have received an enormous amount of attention and interest from both scientific and industrial communities. Artificial dielectric layers (ADL) [1, 2] and artificial magnetic conductors (AMC) [10] are effective to shield the antennas from the lossy Si substrates. A metamaterial antenna using a composite right/left-handed (CRLH) transmission line (TL) in standard CMOS technology was proposed [11]. While the radiation frequency of a standard dipole antenna is determined by the antenna size, the radiation frequency of a CRLH antenna can be controlled by changing element values, which reduces the antenna size [21, 22]. The reduced size can alleviate the influence of the Si substrate and increase the antenna gain.

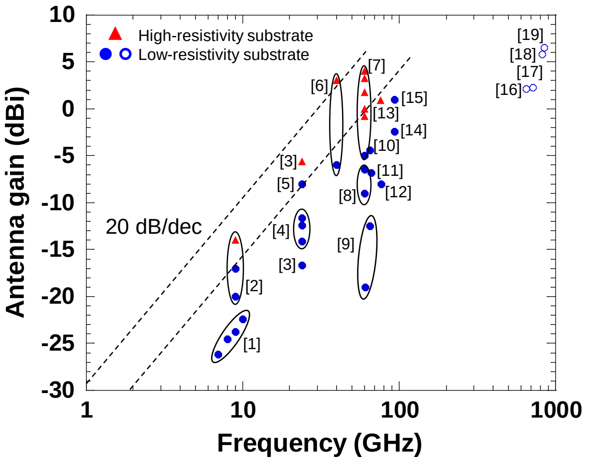

Fig. 1**.** Antenna gain versus frequency characteristics. Solid symbols: measurements. Open symbols: simulations.

The unit cell in a periodic CRLH TL is shown in Fig. 2. Shunt inductors L_L and series capacitors C_L as left-handed elements are inserted in the right-handed transmission line. Applying the periodic boundary condition, the dispersion characteristics for the CRLH TL are described by

$$\beta p = \cos^{-1}\left[1-\frac{1}{2}\left\{\left(\omega L_R - \frac{1}{\omega C_L}\right)\cdot\left(\omega C_R - \frac{1}{\omega L_L}\right)\right\}\right], \tag{1}$$

where β is the phase constant and p is the length of a unit cell [23]. A schematic dispersion diagram of the CRLH TL is shown in Fig. 3.

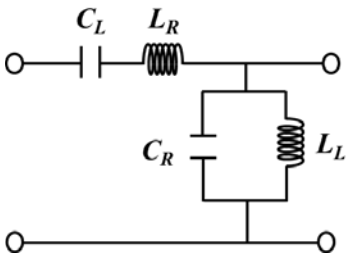

Fig. 2. Unit cell of CRLH TL.

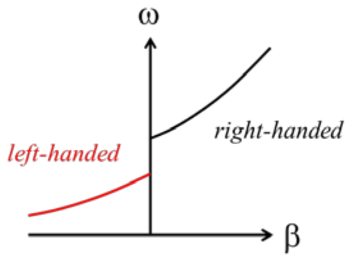

Fig. 3. Dispersion diagram of CRLH TL.

The structure of a metamaterial dipole antenna composed of 4 CRLH cells is shown in Figure 3. Since both ends of the lines are open, the amount of phase change between the two open ends must be π at the target frequency. This means that βp must equal π/4 in the 4-cell configuration.

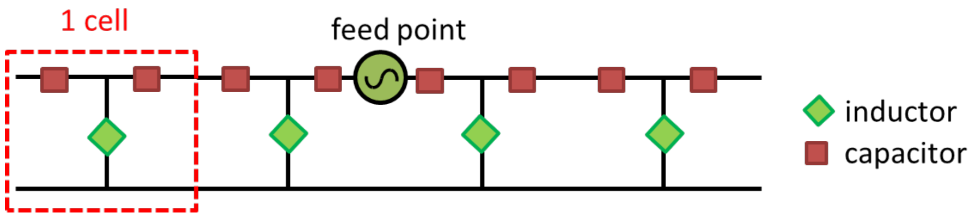

Fig. 4. Structure of metamaterial antenna.

A CRLH monopole antenna was implemented by using this concept in 180-nm CMOS with six metal layers. Series capacitors C_L were composed of metal-insulator-metal (MIM) capacitors between metal 5 and metal 6. The parallel inductor L_L was implemented only by a straight line of metal 6. The RH part of the CRLH monopole antenna was formed of a parallel line without a ground plane under the line to prevent a possible reduction in the antenna gain caused by the eddy current flowing in the ground plane. The antenna was designed with a finite-difference time-domain (FDTD) electromagnetic simulator (Keysight Technologies, EMPro). Figure 5 shows a die photograph of the fabricated antenna. The CRLH unit cell was 300 × 420 μm.

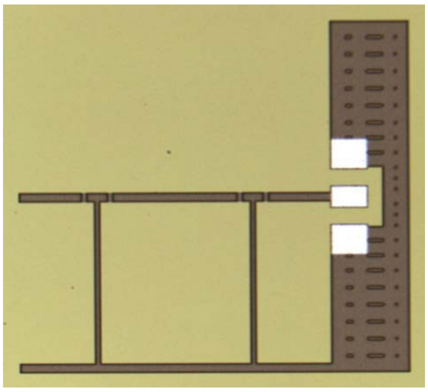

Fig. 5. Die photograph of fabricated antenna.

The fabricated CRLH monopole antenna on a chip was measured using a vector network analyzer (VNA) and a RF probe. A standard 1-port calibration method was used for the return loss measurement. The antenna gain was measured using the VNA and two types of horn antennas (20–40 GHz and 50–67 GHz ranges). Port 1 of the VNA was connected to one of the fabricated antennas, and port 2 of the VNA was connected to the horn antenna. The gain of the CRLH monopole antenna in each frequency range was evaluated by taking into account the transmission S_{21} between two horn antennas and the gain of the horn antenna. Figure 6(a) shows the measured and simulated return losses for the antenna. The designed impedance matching frequencies ($|S_{11}|$) of the LH and RH modes were about 28 GHz (–14.4 dB) and 62 GHz (–6.7 dB), respectively. The measured return loss was shifted about 3 to 6 GHz to a higher frequency compared with the simulated one. Figure 6(b) shows the measured and simulated antenna gains. The measured gains were –14.4 dBi at 39.3 GHz and –5.8 dBi at 66.7 GHz in LH mode and RH mode, respectively. Although the measured gain almost matched the designed gain, the measured gain was ~7 dB smaller than the simulation in the 50–67 GHz range. This might be caused by the different radiation pattern between the horn antenna and the fabricated antenna and/or the difference between fabricated silicon substrate resistivity and the value (10 Ω-cm) assumed in the simulations. The measured gain is plotted in Fig. 1. It is still lower than those of antennas on high-resistivity substrates.

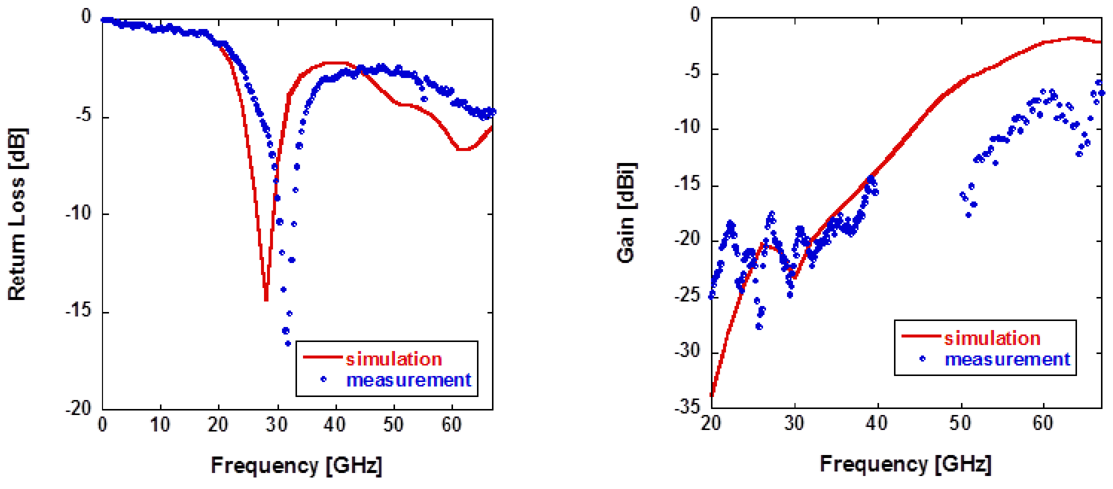

(a) (b)

Fig. 6. Measurement results of fabricated antenna.

The degradation in the gains of antennas on low-resistivity substrates can be alleviated in the submillimeter-wave (or terahertz-frequency) region. Figure 7 shows the calculated maximum efficiency and the optimum radius of circular patch antennas composed of top metal (patch), bottom metal (ground), and 10-μm thick SiO_2. The Si substrate is shielded by the bottom metal. The maximum efficiency reaches 0.5 at 1 THz, and the radius is decreased to 50 μm.

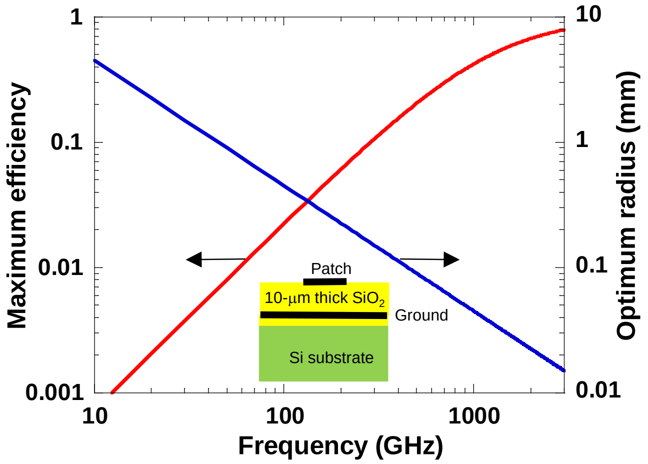

Fig. 7. Calculated maximum efficiency and optimum radius of circular patch antennas.

The terahertz-frequency region (100 GHz – 10 THz), namely, between millimeter-waves and far-infrared light waves, has attracted much attention owing to its wide range of applications (such as wireless communications and sensors). Terahertz waves, which pass through a wide variety of substances, such as plastics, fabrics, and paper, can reveal hidden contents that cannot be seen by visible lights [24]-[26]. In addition, so-called fingerprint spectra in the terahertz frequencies can identify hazardous materials [24]. However, the lack of low-cost and small-size microelectronics that generate sufficient power and detect faint signal (often called the “THz gap”) is one of the major obstacles preventing terahertz applications from coming into wide use in our daily lives [27]. In the microelectronics community, terahertz detection outperforms terahertz generation. Detection methods are generally divided into two methods, namely, coherent (heterodyne) detection and incoherent (direct) detection. Although heterodyne detection achieves higher sensitivity than direct detection, it requires a local oscillator and mixer that are difficult to construct with today’s technology, even if a sub-harmonic scheme is used. For that reason, direct detection has been used. Terahertz direct detectors have primarily relied on specialized fabrication technologies such as Schottky diodes [28], bolometers [29], and high-electron-mobility transistors [30]. Many of these technologies require additional process steps to make them compatible with CMOS technologies [31]. Silicon-CMOS process technologies are becoming a cost-efficient alternative. The main advantage of silicon technologies is that they allow low-cost and large-scale integration of circuits with readout electronics and on-chip signal processors [32]. Furthermore, the high-frequency capabilities of silicon technologies have steadily improved through the guiding principle of scaling, which enables high integration level and low power consumption at higher frequencies [33]. A CMOS cascode amplifier biased near the threshold voltage of a MOSFET was proposed to increase the responsivity of terahertz direct detectors [19].

A block diagram of the terahertz imaging pixel –composed of a microstrip patch antenna, matching circuit, and detector– is shown in Fig. 8.

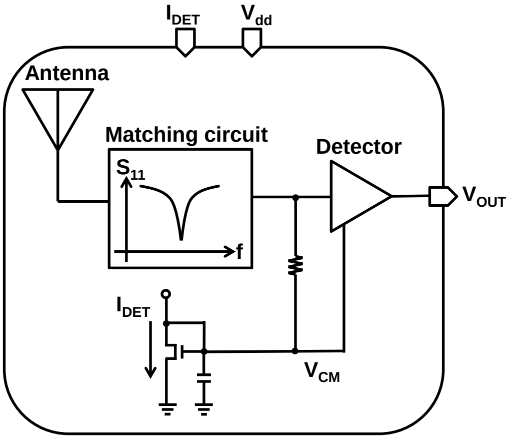

Fig. 8. Block diagram of the terahertz imaging pixel.

For terahertz-wave detection, non-linearity of an nMOSFET was utilized. The nMOSFET was biased near the threshold voltage. The circuit shown in Fig. 9 was used as an envelope detector. It consists of a cascode-amplifier circuit and a subthreshold-biased operational amplifier (subVth-OP amp). The former consists of a common-source nMOSFET M3 as the input stage driven by terahertz signal V_{IN} with common-gate MOSFET M2. And pMOSFET M1 is the load. The cascode-amplifier circuit operates as an envelope detector. The subVth-OP amp operates as a feedback circuit, which determines the load resistance of M1 [34]. Output voltage of the detector is fixed to common-mode voltage VCM at the DC level. Since the subVth-OP amp operates very slowly with a large time constant, the feedback operation is established only at DC and very low frequencies. The feedback circuit operates as a high-pass filter in the detector. Therefore, the envelope detector with the feedback subVth-OP amp produces no DC offset voltage in its output.

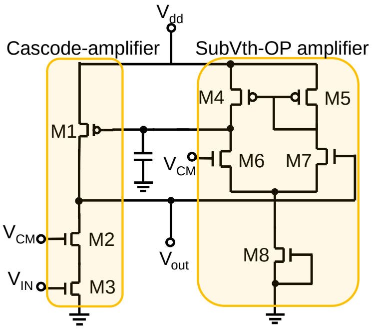

Fig. 9. Schematic of detector circuit.

Each pixel was equipped with a microstrip patch antenna formed by a metal-6 layer (top aluminum layer) and a ground plane (metal-1 layer) in the 180-nm CMOS technology. The dimensions of the antenna were determined with a FDTD electromagnetic simulator (Keysight Technologies, EMPro). The designed gain was 6.5 dBi at 0.85 THz. The antenna size was 130×148 μm. A microstrip line was used for the impedance-matching circuit because it is difficult to use spiral inductors and metal-insulator-metal capacitors in the terahertz region. The width and length of the microstrip line were respectively 5 and 41 μm. A die photo of the fabricated imaging array is shown in Fig. 10. It consists of a 4×4 pixel array and 2-bit row/column decoders. The total size of the circuit is 1035×745 μm. A single pixel occupies 180×250 μm.

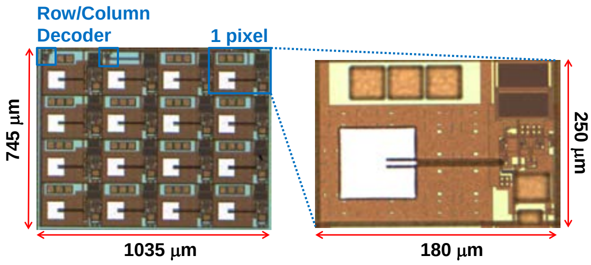

Fig. 10. Die photo of fabricated imaging array.

An injection-seeded terahertz-wave parametric generator (is-TPG) was used as a frequency-tunable terahertz-wave source [35]. By changing the noncollinear phase-matching condition in $MgO:LiNbO_3$ crystal, the terahertz-wave frequency was continuously tuned from 0.8 to 1.1 THz with a linewidth of approximately 4 GHz. At the frequency of 0.905 THz, the terahertz-wave pulse energy was measured to be 132 nJ/pulse with a repetition rate of 100 Hz, corresponding to the average power of 13.2 μW. According to the measured terahertz-wave beam profile, the average power irradiated to the microstrip patch antenna was estimated to be 4.96 nW. Terahertz-wave output was modulated at 31 Hz by an optical chopper, and lock-in detection with 10-100 Hz bandpass filter was used. The measured responsivity of the fabricated imaging array is plotted in Fig. 11. The responsivity of the pixel was calculated from detected output voltage divided by available power to the antenna. The peak responsivity at

0.915 THz is 51.9 kV/W. And each pixel only draws 1 μA from a power supply (V_{dd}) of 1.5 V. Although the peak frequency shifted from 850 to 0.915 THz, the measured responsivity was close to the designed responsivity. Thus, the gain of the microstrip patch antenna was estimated to be close to the designed value of 6.5 dBi. The double-peak property in the measured responsivity is under investigation.

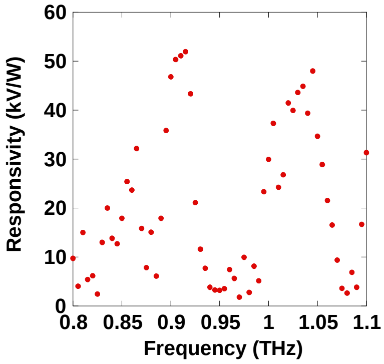

Fig. 11. Measured responsivity.

At modulation frequency of 31 Hz, output noise level was 18.6 μV/Hz$^{1/2}$, and measured noise equivalent power (NEP) was 358 pW/Hz$^{1/2}$. NEP can be decreased by increasing sampling rate. Since the measured imaging array excluded an output buffer, the operation bandwidth of the detector with the extremely small current was degraded by the parasitic capacitances in the measurement equipment. The operation bandwidth can be increased by introducing an output buffer. By introducing an output buffer for each column (or row) and increasing sampling rate, NEP of 42 pW/Hz$^{1/2}$ is expected to be obtained at 10 kHz. These results suggest that cost-efficient terahertz imaging is possible.

References

[1] K. Takahagi, M. Ohno, M. Ikebe, and E. Sano, “Ultra-wideband silicon on-chip antennas with artificial dielectric layer,” *2009 Inter’l Symp. on Intelligent Signal Processing and Communication Systems*, December 7–9, MP1-A-1, 2009.

[2] K. Takahagi and E. Sano, “High-gain silicon on-chip antenna with artificial dielectric layer,” *IEEE Trans. Antennas Propag.*, vol. 59, no. 10, pp. 3624–3629, 2011.

[3] A. B. M. Harun-ur Rashid, S. Watanabe, and T. Kikkawa, “Characteristics of Si integrated antenna for inter-chip wireless interconnection,” *Jpn. J. Appl. Phys.*, vol. 43, pp. 2283–2287, 2004.

[4] J. Lin, L. Gao, A. Sugavanam, X. Guo, R. Li, J. E. Brewer, and K. K. O, “Integrated antennas on silicon substrates for communication over free space,” *IEEE Electron Device Lett.*, vol. 25, no. 4, pp. 196–198, 2004.

[5] A. Shamim, L. Roy, N. Fong, and N. G. Tarr, “24 GHz on-chip antennas and balun on bulk Si for air transmission,” *IEEE. Trans. Antennas Propag.*, vol. 56, no. 2, pp. 303–311, 2008.

[6] K. T. Chan *et al*., “Integrated antennas on Si with over 100 GHz performance, fabricated using an optimized

proton implantation process," *IEEE Microw. Wireless Compon. Lett.*, vol. 13, pp. 487–489, 2003.

[7] Y. P. Zhang, M. Sun, and W. Fan, "Performance of integrated antennas on silicon substrates of high and low resistivities up to 110 GHz for wireless interconnects," *Microwave Opt. Technol. Lett.*, vol. 48, no. 2, pp. 302–305, 2006.

[8] Y. P. Zhang, L. H. Guo, and M. Sun, "High transmission gain inverted-F antenna on low-resistivity Si for wireless Iinterconnect," *IEEE Electron Device Lett.*, vol. 27, no. 5, pp. 374–376, 2006.

[9] Y. P. Zhang, M. Sun, and L. H. Guo, "On-chip antennas for 60-GHz radios in silicon technology," *IEEE Trans. Electron Devices*, vol. 52, no. 7, pp. 1664–1668, 2005.

[10] X. –Y. Bao, Y. –X. Guo, and Y. –Z. Xiong, "60-GHz AMC-based circularly polarized on-chip antenna using standard 0.18-μm CMOS Technology," *IEEE. Trans. Antennas Propag.*, vol. 60, no. 5, pp. 2234–2241, 2012.

[11] K. Hiraishi, T. Kawauchi, and E. Sano, "Millimeter-wave metamaterial antenna in standard CMOS technology," *Progress In Electromagnetics Research Symposium (PIERS) 2015* (Prague, Czech Republic), July 6–9, pp. 483–486, 2015.

[12] A. Babakhani, X. Guan, A. Komijani, A. Natarajan, and A. Hajimiri, "A 77-GHz phased-array transceiver with on-chip antennas in Silicon: Receiver and antennas," *IEEE J. Solid-State Circuits*, vol. 41, no. 12, pp. 2795–2806, 2006.

[13] M. Singer, K. M. Strohm, J. -F. Luy, E. M. Biebl, "Active SIMMWIC- antenna for automotive applications," *IEEE MTT-S Digest*, pp. 1265-1268, 1997.

[14] S. Pan, F. Caster, P. Heydari, and F. Capolino, "A 94-GHz extremely thin metasurface-based BiCMOS on-chip antenna," *IEEE. Trans. Antennas Propag.*, vol. 62, no. 9, pp. 4439–4451, 2014.

[15] S. Pan, L. Gilreath, P. Heydari, and F. Capolino, "Investigation of a wideband BiCMOS fully on-chip W-band bowtie slot antenna," *IEEE Antennas Wireless Propag. Lett.*, vol. 12, pp. 706–709, 2013.

[16] E. Öjefors, U. R. Pfeiffer, A. Lisauskas, and H. G. Roskos, "A 0.65 THz focal-plane array in a quarter-micron CMOS process technology," *IEEE J. Solid-State Circuits*, vol. 44, no. 7, pp. 1968–1976, 2009.

[17] A. S. Abdellatif, A. Taeb, S. Safavi-Naeini, and K. Schmalz, "A terahertz high-efficiency on-chip antenna," *2014 IEEE APS Int'l Symp. (APSURSI)*, pp. 1485–1486, 2014.

[18] D. Y. Kim, S. Park, R. Han, and K. K. O, "820-GHz imaging array using diode-connected NMOS transistors in 130-nm CMOS," *Dig. Tech. Papers 2013 IEEE VLSI Circuits Symp.*, (Kyoto, Japan), pp. 12–13, June 2013.

[19] K. Wakita, E. Sano, M. Ikebe, S. Arnold, T. Otsuji, Y. Takida, and H. Minamide, "Design and fabrication of a terahertz imaging array in 180-nm CMOS process technology," *21st Int'l Conf. Microwaves, Radar and Wireless Communications (MIKON 2016)* (Krakow, Poland), May 9–11, paper M4.3, 2016.

[20] J. B. Pendry, "Negative refraction makes a perfect lens," *Phys. Rev. Lett.*, vol. 85, no. 18, pp. 3966–3969, 2000.

[21] K. Takahagi, Y. Otsu, and E. Sano, "2.45 GHz high-gain electrically small antenna with composite right/left-handed ladder structure," *Electron. Lett.*, vol. 48, no. 16, pp. 971–972, 2012.

[22] K. Hiraishi, T. Wada, Y. Otsu, M. Ikebe, and E. Sano, "Low-power, small-size transmitter module with

metamaterial antenna," *Analog Integr. Circ. Sig. Process.*, vol. 83, no. 1, pp. 1–9, 2015.

[23] C. C. Caloz, A. Sanada, and T. Itoh, "A novel composite right-/left-handed coupled-line directional coupler with arbitrary coupling level and broad bandwidth," *IEEE Trans. Microwave Theory Tech*., vol. 52, no. 3, pp. 980–992, 2004.

[24] K. Kawase *et al*., "Non-destructive terahertz imaging of illicit drugs using spectral fingerprints," *Opt. Express*, vol. 11, pp. 2549–2554, 2003.

[25] M. C. Kemp *et al*., "Security applications of terahertz technology," *Proc. SPIE*, vol. 5070, pp. 44–52, 2003.

[26] B. Zhu *et al*., "Terahertz science and technology and applications," *PIERS Proc.*, Beijing, China, pp. 1166–1170, March 2009.

[27] A. Hellicar *et al*., "Development of a terahertz imaging system," *IEEE AP-S Internatinal Symposium*, pp. 5535–5538, 2007.

[28] J. L. Hesler and T. W. Crowe, "Responsivity and noise measurements of zero-bias Schottky diode detectors," *Proc. 18th International Symposium on Space Terahertz Technology*, pp. 89–92, 2007.

[29] P. Helisto *et al*., "Antenna-coupled microbolometers for passive THz direct detection imaging arrays," *Proc. 1st European Microwave Integrated Circuits Conference*, pp. 35–38, 2006.

[30] L. Samoska, "An overview of solid-state integrated circuit amplifiers in the submillimeter-wave and THz regime," *IEEE Trans. Terahertz Sci. Technol.*, vol. 1, pp. 9–24, 2011.

[31] S. Eminoglu, M. Tanrikulu, and T. Akin, "A low-cost 128 x 128 uncooled infrared detector array in CMOS process," J. Microelectromechanical Systems, vol. 17, pp. 20–30, 2008.

[32] E. Öjefors *et al*., "Terahertz imaging detectors in CMOS technology," *J. Infrared Milli. Terahz. Waves*, vol. 30, pp. 1269–1280, 2009.

[33] R. A. Hadi *et al*., "A 1 k-pixel video camera for 0.7-1.1 terahertz imaging applications in 65-nm CMOS," *IEEE J. Solid-State Circuits*, vol. 47, no. 12, pp. 2999–3012, 2012.

[34] T. Wada, M. Ikebe, and E. Sano, "60-GHz, 9 μW wake-up receiver for short-range wireless communications," *Proc. Eur. Solid-State Circuits Conf. (ESSCIRC)*, pp. 383–386, 2013.

[35] S. Hayashi *et al*., "Ultrabright continuously tunable terahertz-wave generation at room temperature," *Scientific Reports*, vol. 4, p. 5045, 2014.

D6. Space-Division-Multiplexed Optical Fiber Transmission

Hiroyuki Toda
Doshisha University

In this section, I summarize recent development of high capacity optical fiber transmission using space-division-multiplexing (SDM) techniques and related technologies, reported during the period from November 2013 to October 2016. There has been significant interest in SDM techniques realized by MCF and FMF, since it is expected to improve transmission capacity per fiber drastically.

In [1], 31-core MCF was developed for up to 4,000km transmission. In [2-5], MCFs with 125-μm cladding, which are compatible with conventional fibers, were developed. In [6], transmission systems consist of homogeneous single-mode MCF, where each core has the same parameter, were discussed. [7, 8] demonstrated crosstalk reduction with bidirectional signal assignment in MCF, and showed possibility of gradual upgrade of SMF-based line to MCF-based line. Heterogeneous MCFs to reduce inter-core crosstalk with 30 cores [9] and 32 cores [10] were demonstrated.

Coupled-core (CC) MCF described in [11-14] is another type of MCF, which permits strong mode coupling between cores, thus allowing smaller core-to-core distance and higher spatial efficiency compared to uncoupled MCFs. CC-MCF also shows low DGD between spatial modes (SMD), which results in reducing MIMO-DSP complexity, and therefore attractive for long-haul transmission. [15] demonstrated 4-core 125 μm cladding CC-MCF with 0.158 dB/km propagation loss and 6.1 ps/km$^{1/2}$ SMD. [13] also demonstrated strongly-coupled 3-mode 7-core FM-MCF.

In order to further increase the transmission capacity, combining FMF and MCF technologies, referred as FM-MCF is promising. [16] and [17] review 3-mode 12 core FM-MCF. In [18] and [19], 3-mode 36-core FM-MCF with 306-μm diameter cladding was fabricated. In [20], 6-mode 19-core FM-MCF with 318-μm cladding, and in [21], 6-mode 19-core FM-MCF with 246 μm cladding were demonstrated. It should be noted that spatial channel numbers exceed 100 for those fibers. 6-mode 12-core FM-MCF with 227 μm cladding was fabricated for improving spatial efficiency [22]. [23] demonstrated moderately coupled 2-mode 6-core FM-MCF with 125 μm cladding.

[24-27] review the current state of the MCFs and FM-MCFs.

In order to realize SDM transmission systems, development of SDM component is important. MC-EDFAs were reported in [28, 29]. FM-EDFAs were reported in [30, 31]. Fiber connectors were demonstrated in [32, 33]. Fusion splicing of MCF was demonstrated in [34]. MCF cable was presented in [35]. FI/FO for MCF and mode MUX/DEMUX for FMF are necessary if conventional fiber devices are used. Various types of FI/FO and MUX/DEMUX were proposed and demonstrated in [19, 36-42]. Parameter measurement of MCF and FMF is also important for realizing SDM transmission systems. Measurement techniques for distribution of mode field diameter and refractive index, mode coupling at FMF splicing point, modal crosstalk of FMF, and mode coupling distribution of FMF were proposed and demonstrated in [43], [44], [45] and [46], respectively. In [47], fiber fuse propagation, that limits maximum launched power to the fiber, in FMF was observed and examined.

Many transmission experiment using MCF or FM-MCF were reported. Using 7-core EDFA and 7-core MCF, 120.7 Tbit/s (7-SDM 180-WDM 95.8 Gb/s) 204 km transmission [48], and 51.1 Tbit/s 2,520 km transmission [49, 50] were demonstrated. 2.15 Pbit/s 31 km transmission was demonstrated using 22-core MCF in [51]. In [52], 20-WDM PDM-16QAM 96 Gbit/s signals were transmitted over 1,600 km using low-crosstalk heterogeneous 32-core MCF. The aggregate spectral efficiency was 201.46 bit/s/Hz. In [53], 1,200 km transmission experiment was made using 19-core EDFA and 19-core MCF.

Transmission capacity can be further improved by using FM-MCF. In [54], 20-WDM PDM-32QAM 105 Gbit/s signals were transmitted over 40 km using 3-mode 12-core FM-MCF. The aggregate spectral efficiency was 247.9 bit/s/Hz. In [55, 56], 20-WDM PDM-QPSK 40 Gbit/s signals were transmitted over 527 km with 3-mode 12-core FM-MCF. In [18] and [19], 403.7 Tbit/s 5.5 km transmission was demonstrated using 3-mode 36-core FM-MCF. Using 9.8-km 6-mode 19-core MCF, 140.7 Tbit/s 7,300 km transmission were demonstrated by using super Nyquist WDM [57]. Spectral efficiency of 345 bit/s/Hz was obtained in [58]. 2.05 Pbit/s transmission was demonstrated in [59, 60]. The spectral efficiency was improved by 947 bit/s/Hz by using DP-64QAM modulation format [61].

SDM transmission technologies were reviewed in [62-69].

List of Abbreviations

DGD	Differential group delay
DP	Dual polarization
DSP	Digital signal processing
EDFA	Erbium-doped fiber amplifier
FI/FO	Fan-in/fan-out
FMF	Few-mode fiber
FM-MCF	Few-mode multicore fiber
MCF	Multicore fiber
MIMO	Multiple-input multiple-output
MUX/DEMUX	Multiplexer/demultiplexer
PDM	Polarization-division multiplexing
QAM	Quadrature amplitude modulation
QPSK	Quadrature phase-shift keying
SMF	Single-mode fiber
WDM	Wavelength-division multiplexing

References

[1] Tetsuya Nakanishi, Tetsuya Hayashi, Osamu Shimakawa, and Takashi Sasaki,

"Spatial-Spectral-Efficiency-enhanced Multi-Core Fiber," Tech. Digest of OFC 2015, Th3C.3, Los Angeles, Mar. 22-26, 2015.

[2] Tetsuya Hayashi, Tetsuya Nakanishi, Kaoru Hirashima, Osamu Shimakawa, Fumiaki Sato, Koichi Koyama, Akira Furuya, Yasunori Murakami, and Takashi Sasaki, "125-μm-Cladding 8-Core Multi-Core Fiber Realizing Ultra-High-Density Cable Suitable for O-Band Short-Reach Optical Interconnects, " Tech. Digest of OFC 2015, Th5C.6, Los Angeles, Mar. 22-26, 2015.

[3] Tetsuya Hayashi, Tetsuya Nakanishi, Kaoru Hirashima, Osamu Shimakawa, Fumiaki Sato, Koichi Koyama, Akira Furuya, Yasunori Murakami, and Takashi Sasaki, "125-μm-Cladding Eight-Core Multi-Core Fiber Realizing Ultra-High-Density Cable Suitable for O-Band Short-Reach Optical Interconnects," Journal of Lightwave Technology, vol. 34, no. 1, pp. 85-92, 2016.

[4] Takashi Matsui, Taiji Sakamoto, Yukihiro Goto, Kotaro Saito, Kazuhide Nakajima, Fumihiko Yamamoto, and Toshio Kurashima, "Design of 125 μm cladding multi-core fiber with full-band compatibility to conventional single-mode fiber," Tech Digest of ECOC 2015, We.1.4.5, Valencia, Sept. 27-Oct. 1, 2015.

[5] Tomohiro Gonda, Katsunori, Imamura, Ryuichi Sugizaki, Yu Kawaguchi, and Takehiro Tsuritani, "125 μm 5-core fibre with heterogeneous design suitable for migration from single-core system to multi-core system," Tech Digest of ECOC 2016, W.2.B.1, Düsseldorf, Sept. 18-22, 2016.

[6] B. J. Puttnam, R. S. Luis, J. Sakaguchi, W Klaus, J-M, Delgado Mendinueta, Y. Awaji, N. Wada, and E. Agrell, "Pb/s, Homogeneous, Single-mode, Multi-Core Fiber Systems," Tech Digest of ECOC 2016, Tu.1.D.2, Düsseldorf, Sept. 18-22, 2016.

[7] Manabu Arikawa, Toshiharu Ito, Emmanuel Le Taillandier de Gabory, and Kiyoshi Fukuchi, "Crosstalk Reduction Using Bidirectional Signal Assignment over Square Lattice Structure 16-Core Fiber for Gradual Upgrade of SSMF-Based Lines," Tech Digest of ECOC 2015, Th.1.2.3, Valencia, Sept. 27-Oct. 1, 2015.

[8] Manabu Arikawa, Toshiharu Ito, Emmanuel Le Taillandier de Gabory, and Kiyoshi Fukuchi, "Crosstalk Reduction With Bidirectional Signal Assignment on Square Lattice Structure 16-Core Fiber Over WDM Transmission for Gradual Upgrade of SMF-Based Lines," Journal of Lightwave Technology, vol. 34, no. 8, pp. 1908-1915, 2016.

[9] K. Takenaga, S. Matsuo, K. Saitoh, T. Morioka, and Y. Miyamoto, "High-Density Multicore Fibers," Tech. Digest of OFC 2016, W1F.1, Anaheim, Mar. 20-24, 2016.

[10] Yusuke Sasaki, Ryohei Fukumoto, Katsuhiro Takenaga and Kazuhiko Aikawa, "Crosstalk-Managed Heterogeneous Single-Mode 32-Core Fibre," Tech Digest of ECOC 2016, W.2.B.2, Düsseldorf, Sept. 18-22, 2016.

[11] R. Ryf, N. K. Fontaine, M. Montoliu, S. Randel, S. H. Chang, H. Chen, S. Chandrasekhar, A. H. Gnauck, R. -J. Essiambre, P. J. Winzer, T. Taru, T. Hayashi, T. Sasaki, "Space-Division Multiplexed Transmission Over 3 × 3 Coupled-Core Multicore Fiber," Tech. Digest of OFC 2014, Tu2J.4, San Francisco, Mar. 9-14, 2014.

[12] Tetsuya Hayashi, Roland Ryf, Nicolas K. Fontaine, Cen Xia, Sebastian Randel, René-Jean Essiambre, Peter J. Winzer, and Takashi Sasaki, "Coupled-Core Multi-Core Fibers: High-Spatial-Density Optical Transmission

Fibers with Low Differential Modal Properties," Tech Digest of ECOC 2015, We.1.4.1, Valencia, Sept. 27-Oct. 1, 2015.

[13] T. Sakamoto, T. Mori, M. Wada, T. Yamamoto, F. Yamamoto, and K. Nakajima, "Coupled Few-mode Multi-core Fibre for Ultra-high Spatial Density Space Division Multiplexing," Tech Digest of ECOC 2016, W.2.B.3, Düsseldorf, Sept. 18-22, 2016.

[14] Tetsuya Hayashi, Haoshuo Chen, Nicolas K. Fontaine, Takuji Nagashima, Roland Ryf, René-Jean Essiambre, and Toshiki Taru, "Effects of Core Count/Layout and Twisting Condition on Spatial Mode Dispersion in Coupled Multi-Core Fibers," Tech Digest of ECOC 2016, W.2.B.5, Düsseldorf, Sept. 18-22, 2016.

[15] Tetsuya Hayashi, Yoshiaki Tamura, Takemi Hasegawa, and Toshiki Taru, "125-μm-cladding Coupled Multi-core Fiber with Ultra-low Loss of 0.158 dB/km and Record-low Spatial Mode Dispersion of 6.1 ps/km$^{1/2}$," Tech. Digest of OFC 2016, Th5A.1, Anaheim, Mar. 20-24, 2016.

[16] Yusuke Sasaki, Yoshimichi Amma, Katsuhiro Takenaga, Shoichiro Matsuo, Kunimasa Saitoh and Masanori Koshiba, "Few-mode Multicore Fibre with 36 Spatial Modes (Three modes (LP_{01}, LP_{11a}, LP_{11b}) × 12 cores)," Tech Digest of ECOC 2014, Th.1.4.1, Cannes, Sept. 21-25, 2014.

[17] Yusuke Sasaki, Yoshimichi Amma, and Katsuhiro Takenaga, "Few-mode multicore fibre with 36 spatial modes (Three modes (LP_{01}, LP_{11a}, LP_{11b}) × 12 cores)," Journal of Lightwave Technology, vol. 33, no. 5, pp. 964-970, 2015.

[18] Jun Sakaguchi, Werner Klaus, Jose Manuel Delgado Mendinueta, Benjamin J. Puttnam, Ruben S. Luis, Yoshinari Awaji, Naoya Wada, Tetsuya Hayashi, Tetsuya Nakanishi, Tatsuhiko Watanabe, Yasuo Kokubun, Taketoshi Takahata, and Tetsuya Kobayashi, "Realizing a 36-core, 3-mode Fiber with 108 Spatial Channels," Tech. Digest of OFC 2015, Th5C.2, Los Angeles, Mar. 22-26, 2015.

[19] Jun Sakaguchi, Werner Klaus, José Manuel Delgado Mendinueta, Benjamin James Puttnam, Ruben Soares Luís, Yoshinari Awaji, Naoya Wada, Tetsuya Hayashi, Tetsuya Nakanishi, Tatsuhiko Watanabe, Yasuo Kokubun, Taketoshi Takahata, and Tetsuya Kobayashi, "Large Spatial Channel (36-Core × 3 mode) Heterogeneous Few-Mode Multicore Fiber," Journal of Lightwave Technology, vol. 34, no. 1, pp. 93-103, 2016.

[20] Tetsuya Hayashi, Takuji Nagashima, Kazuhiro Yonezawa, Yuta Wakayama, Daiki Soma, Koji Igarashi, Takehiro Tsuritani, and Takashi Sasaki, "6-mode 19-core Fiber for Weakly-coupled Mode-multiplexed Transmission over Uncoupled Cores," Tech. Digest of OFC 2016, W1F.4, Anaheim, Mar. 20-24, 2016.

[21] T. Sakamoto, T. Matsui, K. Saitoh, S. Saitoh, K. Takenaga, T. Mizuno, Y. Abe, K. Shibahara, Y. Tobita, S. Matsuo, K. Aikawa, S. Aozasa, K. Nakajima, Y. Miyamoto, "Low-loss and Low-DMD Few-mode Multi-core Fiber with Highest Core Multiplicity Factor," Tech. Digest of OFC 2016, Th5A.2, Anaheim, Mar. 20-24, 2016.

[22] Taiji Sakamoto, Takashi Matsui, Kunimasa Saitoh, Shota Saitoh, Katsuhiro Takenaga, Shoichiro Matsuo, Yuki Tobita, Nobutomo Hanzawa, Kazuhide Nakajima, and Fumihiko Yamamoto, "Few-mode Multi-core Fibre with Highest Core Multiplicity Factor," Tech Digest of ECOC 2015, We.1.4.3, Valencia, Sept. 27-Oct.

1, 2015.

[23] Taiji Sakamoto, Takayoshi Mori, Takashi Yamamoto, Masaki Wada, Fumihiko Yamamoto, “Moderately Coupled 125-μm Cladding 2 LP-mode 6-core Fiber for Realizing Low MIMO-DSP and High Spatial Density,” Tech Digest of ECOC 2014, Tu.4.1.3, Cannes, Sept. 21-25, 2014.

[24] Kunimasa Saitoh, “Multicore Fiber Technology,” Tech. Digest of OFC 2015, Th4C.1, Los Angeles, Mar. 22-26, 2015.

[25] Kunimasa Saitoh, and Shoichiro Matsuo, “Multicore Fiber Technology,” Journal of Lightwave Technology, vol. 34, no. 1, pp. 55-66, 2016.

[26] Shoichiro Matsuo, Katsuhiro Takenaga, Kunimasa Saitoh, Kazuhide Nakajima, Yutaka Miyamoto, and Toshio Morioka, “High-Spatial-Multiplicity Multi-Core Fibres for Future Dense Space-Division-Multiplexing System,” Tech Digest of ECOC 2015, Th.1.2.1, Valencia, Sept. 27-Oct. 1, 2015.

[27] Shoichiro Matsuo, , Katsuhiro Takenaga, Yusuke Sasaki, Yoshimichi Amma, Shota Saito, Kunimasa Saitoh, , Takashi Matsui, Kazuhide Nakajima, Takayuki Mizuno, Hidehiko Takara, Yutaka Miyamoto, and Toshio Morioka, “High-Spatial-Multiplicity Multicore Fibers for Future Dense Space-Division-Multiplexing Systems,” Journal of Lightwave Technology, vol. 34, no. 6, pp. 1464-1475, 2016.

[28] Yukihiro Tsuchida, Masateru Tadakuma, and Ryuichi Sugizaki, “Multicore EDFA for Space Division Multiplexing by Utilizing Cladding-pumped Technology,” Tech. Digest of OFC 2014, Tu2D.1, San Francisco, Mar. 9-14, 2014.

[29] Y. Tsuchida, K. Maeda, K. Watanabe, K. Takeshima, T. Sasa, T. Saito, S. Takasaka, Y. Kawaguchi, T. Tsuritani, and R. Sugizaki, “Cladding Pumped Seven-Core EDFA Using an Absorption-Enhanced Erbium Doped Fibre,” Tech Digest of ECOC 2016, M.2.A.2, Düsseldorf, Sept. 18-22, 2016.

[30] Masaki Wada, Taiji Sakamoto, Shinichi Aozasa, Takayoshi Mori, Takashi Yamamoto, and Kazuhide Nakajima, “Differential modal gain reduction of L-band 5-spatial mode EDFA with depressed core structure,” Tech. Digest of OFC 2016, Tu2I.4, Anaheim, Mar. 20-24, 2016.

[31] Yuta Wakayama, Koji Igarashi, Daiki Soma, Hidenori Taga, and Takehiro Tsuritani, “Novel 6-Mode Fibre Amplifier with Large Erbium-Doped Area for Differential Modal Gain Minimization,” Tech Digest of ECOC 2016, M.2.A.3, Düsseldorf, Sept. 18-22, 2016.

[32] Kengo Watanabe, Tsunetoshi Saito, Katsuki Suematsu, Ryo Nagase, Masato Shiino, “Development of small MT type 2-multicore fiber connector,” Tech. Digest of OFC 2014, W4D.6, San Francisco, Mar. 9-14, 2014.

[33] Ryo Nagase, “How to Connect Multicore and Multimode Fibers,” Tech. Digest of OFC 2014, Tu3D.2, San Francisco, Mar. 9-14, 2014.

[34] Kotaro Saito, Taiji Sakamoto, Takashi Matsui, Kazuhide Nakajima, and Toshio Kurashima, “Side-view based angle alignment technique for multi-core fiber,” Tech. Digest of OFC 2016, M3F.3, Anaheim, Mar. 20-24, 2016.

[35] Itaru Ishida, Yoshimichi Amma, Keisuke Hirakawa, Hitoshi Uemura, Yusuke Sasaki, Katsuhiro Takenaga,

Naoto Itou, Ken Osato and Shoichiro Matsuo, “Multicore-fiber Cable with Core Density of 6 cores/mm^2,” Tech. Digest of OFC 2014, W4D.3, San Francisco, Mar. 9-14, 2014.

[36] Yusaku Tottori, Hiroshi Tsuboya and Tetsuya Kobayashi, “Multi Functionality Demonstration for Multi Core Fiber Fan-in/Fan-out Devices using Free Space Optics,” Tech. Digest of OFC 2014, Th2A.44, San Francisco, Mar. 9-14, 2014.

[37] T. Watanabe and Y. Kokubun, “Fan-in/Fan-out Three-dimensional Polymer Waveguide for Uncoupled Multi-core Fibers,” Tech Digest of ECIO 2014, Tu3bI2, Nice, June 24-27, 2014.

[38] Masato Yoshida, Toshihiko Hirooka, and Masataka Nakazawa, “Fused Type Fan-out Device for Multi-core Fiber Based on Bundled Structure,” Tech. Digest of OFC 2016, Tu3I.2, Anaheim, Mar. 20-24, 2016.

[39] H. Uemura, Y. Sasaki, S. Nishimoto, T. Uematsu, K. Takenaga, K. Omichi, R. Goto, S. Matsuo and K. Saitoh, “Mode Multiplexer/Demultiplexer Based on a Partially Elongated Multi-Core Fiber,” Tech. Digest of OFC 2014, Tu3D.3, San Francisco, Mar. 9-14, 2014.

[40] K. Takenaga, H. Uemura, Y. Sasaki, S. Nishimoto, T. Uematsu, K. Omichi, R. Goto, S. Matsuo, and K. Saitoh, “Multicore fibre-based Mode Multiplexer/Demultiplexer for Three-Mode Operation of LP_{01}, LP_{11a}, and LP_{11b},” Tech Digest of ECOC 2014, Tu.4.1.4, Cannes, Sept. 21-25, 2014.

[41] Daiki Soma, Koki Takeshima, Koji Igarashi and Takehiro Tsuritani, “Degenerate Modes Multiplexer/Demultiplexer using Mach- Zehnder Interferometer with Image Inversion,” Tech Digest of ECOC 2014, We.1.1.6, Cannes, Sept. 21-25, 2014.

[42] Nobutomo Hanzawa, Kunimasa Saitoh, Taiji Sakamoto, Takashi Matsui, Kyozo Tsujikawa, Takui Uematsu, and Fumihiko Yamamoto, “Four-mode PLC-based mode multi/demultiplexer with LP_{11} mode rotator on one chip for MDM transmission,” Tech Digest of ECOC 2014, We.1.1.1, Cannes, Sept. 21-25, 2014.

[43] M. Ohashi, H. Kubota, Y. Miyoshi, R. Maruyama, and N. Kuwaki, “Longitudinal Fiber Parameter Measurements of Two-Mode Fiber Links by using OTDR,” Tech Digest of ECOC 2014, Th.1.4.5, Cannes, Sept. 21-25, 2014.

[44] Masato Yoshida, Toshihiko Hirooka, and Masataka Nakazawa, “Mode Coupling Measurement at a Splice Point between Few- Mode Fibers Using a Synchronous Multi-Channel OTDR,” Tech. Digest of OFC 2016, Th1J.4, Anaheim, Mar. 20-24, 2016.

[45] Takayuki Mizuno, Hidehiko Takara, Manabu Oguma, Takayuki Kobayashi, and Yutaka Miyamoto, "Modal Crosstalk Measurement Based on Intensity Tone for Few-Mode Fiber Transmission Systems,” Tech. Digest of OFC 2014, W3D.5, San Francisco, Mar. 9-14, 2014.

[46] Masataka Nakazawa, Masato Yoshida, and Toshihiko Hirooka, “Measurement of Mode Coupling Distribution Along a Few- Mode Fiber Using a Synchronous Multi-Channel OTDR,” Tech. Digest of OFC 2014, W3D.7, San Francisco, Mar. 9-14, 2014.

[47] Nobutomo Hanzawa, Kenji Kurokawa, Kyozo Tsujikawa, Takayoshi Mori, Masaki Wada, and Fumihiko Yamamoto, “Fiber fuse propagation in LP_{11} mode in few-mode fiber,” Tech. Digest of OFC 2015, W4I.5, Los Angeles, Mar. 22-26, 2015.

[48] H. Takara, T. Mizuno, H. Kawakami, Y. Miyamoto, H. Masuda, K. Kitamura, H. Ono, S. Asakawa, Y. Amma, K. Hirakawa, S. Matsuo, K. Tsujikawa, and M. Yamada, “120.7-Tb/s (7 SDM/180 WDM/95.8 Gb/s) MCF-ROPA Unrepeatered Transmission of PDM-32QAM Channels over 204 km,” Tech Digest of ECOC 2014, PD3.1, Cannes, Sept. 21-25, 2014.

[49] Koki Takeshima, Takehiro Tsuritani, Yukihiro Tsuchida, Koichi Maeda, Tsunetoshi Saito, Kengo Watanabe, Toru Sasa, Katsunori Imamura, Ryuichi Sugizaki, Koji Igarashi, Itsuro Morita, and Masatoshi Suzuki, “51.1-Tbit/s MCF Transmission Over 2,520 km Using Cladding Pumped 7-Core EDFAs,” Tech. Digest of OFC 2015, W3G.1, Los Angeles, Mar. 22-26, 2015.

[50] Koki Takeshima, Takehiro Tsuritani, Yukihiro Tsuchida, Koichi Maeda, Tsunetoshi Saito, Kengo Watanabe, Toru Sasa, Katsunori Imamura, Ryuichi Sugizaki, Koji Igarashi, Itsuro Morita, and Masatoshi Suzuki, “51.1-Tbit/s MCF Transmission Over 2,520 km Using Cladding-Pumped Seven-Core EDFAs,” Journal of Lightwave Technology, vol. 34, no. 2, pp. 761-767, 2016.

[51] B. J. Puttnam, R. S. Luis, W. Klaus, J. Sakaguchi, J.-M. Delgado Mendinueta, Y. Awaji, N. Wada, Yoshiaki Tamura, Tetsuya Hayashi, Masaaki Hirano and J. Marciante, “2.15 Pb/s Transmission Using a 22 Core Homogeneous Single- Mode Multi-Core Fiber and Wideband Optical Comb,” Tech Digest of ECOC 2015, PDP.3.1, Valencia, Sept. 27-Oct. 1, 2015.

[52] T. Mizuno, K. Shibahara, H. Ono, Y.Abe, Y. Miyamoto, F. Ye, T. Morioka, Y. Sasaki, Y. Amma, K. Takenaga, S. Matsuo, K. Aikawa, K. Saitoh, Y. Jung, D. J. Richardson, K. Pulverer, M. Bohn, and M. Yamada, “32-core Dense SDM Unidirectional Transmission of PDM- 16QAM Signals Over 1600 km Using Crosstalk-managed Single-mode Heterogeneous Multicore Transmission Line,” Tech. Digest of OFC 2016, Th5C.3, Anaheim, Mar. 20-24, 2016.

[53] Jun Sakaguchi, Werner Klaus, Benjamin J. Puttnam, José Manuel Delgado Mendinueta, Yoshinari Awaji, Naoya Wada, Yukihiro Tsuchida, Koichi Maeda, Masateru Tadakuma, Katsunori Imamura, Ryuichi Sugizaki, Tetsuya Kobayashi, Yusaku Tottori, Masayuki Watanabe, and R. V. Jensen, “19-core MCF transmission system using EDFA with shared core pumping coupled via free-space optics,” Optics Express, vol. 22, no. 1, pp. 90-95, 2014.

[54] T. Mizuno, T. Kobayashi, H. Takara, A. Sano, H. Kawakami, T. Nakagawa, Y. Miyamoto, Y. Abe, T. Goh, M. Oguma, T. Sakamoto, Y. Sasaki, I. Ishida, K. Takenaga, S. Matsuo, K. Saitoh, and T. Morioka, “12-core × 3-mode Dense Space Division Multiplexed Transmission over 40 km Employing Multi-carrier Signals with Parallel MIMO Equalization,” Tech. Digest of OFC 2014, Th5B.2, San Francisco, Mar. 9-14, 2014.

[55] K. Shibahara, T. Mizuno, H. Takara, A. Sano, H. Kawakami, D. Lee, Y. Miyamoto, H. Ono, M. Oguma, Y. Abe, T. Kobayashi, T. Matsui , R. Fukumoto, Y. Amma, T. Hosokawa, S. Matsuo, K. Saito, H. Nasu, and T. Morioka, “Dense SDM (12-core 3-mode) Transmission over 527 km with 33.2-ns Mode-Dispersion Employing Low-Complexity Parallel MIMO Frequency-Domain Equalization,” Tech. Digest of OFC 2015, Th5C.3, Los Angeles, Mar. 22-26, 2015.

[56] Kohki Shibahara, Takayuki Mizuno, Hidehiko Takara, Akihide Sano, Hiroto Kawakami, Doohwan Lee,

Yutaka Miyamoto, Hirotaka Ono, Manabu Oguma, Yoshiteru Abe, Takayuki Kobayashi, Takashi Matsui, Ryohei Fukumoto, Yoshimichi Amma, Tsukasa Hosokawa, Shoichiro Matsuo, Kunimasa Saitoh, Hitoshi Nasu, and Toshio Morioka, “Dense SDM (12-Core × 3-Mode) Transmission Over 527 km With 33.2-ns Mode-Dispersion Employing Low-Complexity Parallel MIMO Frequency-Domain Equalization,” Journal of Lightwave Technology, vol. 34, no. 1, pp. 196-204, 2016.

[57] Koji Igarashi, Takehiro Tsuritani, Itsuro Morita, Yukihiro Tsuchida, Koichi Maeda, Masateru Tadakuma, Tsunetoshi Saito, Kengo Watanabe, Katsunori Imamura, Ryuichi Sugizaki, and Masatoshi Suzuki, “Super-Nyquist-WDM transmission over 7,326-km seven-core fiber with capacity-distance product of 1.03 Exabit/s·km,” Optics Express, vol. 22, no. 2, pp. 1220-1228, 2014.

[58] Koji Igarashi, Daiki Souma, Yuta Wakayama, Koki Takeshima, Yu Kawaguchi, Takehiro Tsuritani, Itsuro Morita, and Masatoshi Suzuki, “114 Space-Division-Multiplexed Transmission over 9.8-km Weakly-Coupled-6-Mode Uncoupled-19-Core Fibers,” Tech. Digest of OFC 2015, Th5C.4, Los Angeles, Mar. 22-26, 2015.

[59] D. Soma, K. Igarashi, Y. Wakayama, K. Takeshima, Y. Kawaguchi, N. Yoshikane, T. Tsuritani, I. Morita, and M. Suzuki, “2.05 Peta-bit/s super-nyquist-WDM SDM transmission using 9.8-km 6-mode 19-core fiber in full C band,” Tech Digest of ECOC 2015, PDP.3.2, Valencia, Sept. 27-Oct. 1, 2015.

[60] Koji Igarashi, Daiki Soma, Yuta Wakayama, Koki Takeshima, Yu Kawaguchi, Noboru Yoshikane, Takehiro Tsuritani, Itsuro Morita, and Masatoshi Suzuki, “Ultra-dense spatial-division-multiplexed optical fiber transmission over 6-mode 19-core fibers,” Optics Express, vol. 24, no. 10, pp. 10213-10231, 2016.

[61] Daiki Soma, Yuta Wakayama, Shohei Beppu, Koji Igarashi, Takehiro Tsuritani, Hidenori Taga, Itsuro Morita, and Masatoshi Suzuki, “665 and 947 b/s/Hz Ultra-highly Aggregate-Spectral-Efficient SDM/WDM Transmission over 6-Mode 19-Core Fibre Using DP-16QAM/64QAM Signals,” Tech Digest of ECOC 2016, Th.3.C.2, Düsseldorf, Sept. 18-22, 2016.

[62] Akihide Sano, Hidehiko Takara, Takayuki Kobayashi, and Yutaka Miyamoto, “Petabit/s Transmission Using Multicore Fibers,” Tech. Digest of OFC 2014, Tu2J.1, San Francisco, Mar. 9-14, 2014.

[63] Hidenori Takahashi, Koji Igarashi, and Takehiro Tsuritani, “Long-haul Transmission Using Multicore Fibers,” Tech. Digest of OFC 2014, Tu2J.2, San Francisco, Mar. 9-14, 2014.

[64] Akihide Sano, Hidehiko Takara, Takayuki Kobayashi, and Yutaka Miyamoto, “Crosstalk-Managed High Capacity Long Haul Multicore Fiber Transmission With Propagation-Direction Interleaving,” Journal of Lightwave Technology, vol. 32, no. 16, pp. 2771-2779, 2014.

[65] Koji Igarashi, Takehiro Tsuritani, Itsuro Morita, and Masatoshi Suzuki, “Ultra-Long-Haul High-Capacity Super-Nyquist-WDM Transmission Experiment Using Multi-Core Fibers,” Journal of Lightwave Technology, vol. 33, no. 5, pp. 1027-1036, 2015.

[66] Takayuki Mizuno, Hidehiko Takara, Akihide Sano, and Yutaka Miyamoto, “Dense Space Division Multiplexed Transmission over Multi-core and Multi-mode Fiber,” Tech. Digest of OFC 2015, Th1D.2, Los Angeles, Mar. 22-26, 2015.

[67] Takayuki Mizuno, Hidehiko Takara, Akihide Sano, and Yutaka Miyamoto, “Dense Space Division Multiplexing Long Haul Transport System Using Multi-core / Multi-mode Fibre,” Tech Digest of ECOC 2015, Th.1.2.2, Valencia, Sept. 27-Oct. 1, 2015.

[68] Takayuki Mizuno, Hidehiko Takara, Akihide Sano, and Yutaka Miyamoto, “Dense Space-Division Multiplexed Transmission Systems Using Multi-Core and Multi-Mode Fiber,” Journal of Lightwave Technology, vol. 34, no. 2, pp. 582-592, 2016.

[69] Takayuki Mizuno, Hidehiko Takara, Kohki Shibahara, Akihide Sano, and Yutaka Miyamoto, “Dense Space Division Multiplexed Transmission Over Multicore and Multimode Fiber for Long-haul Transport Systems,” Journal of Lightwave Technology, vol. 34, no. 6, pp. 1484-1493, 2016.

D7. Recent research trends in optical access network technologies

Jun-ichi Kani

NTT Corporation

1. Background

One of the backgrounds to trigger recent researches in optical access is the rapid progress of the mobile wireless access services. To fundamentally increase the bandwidth in the mobile access, dense deployment of small sells is an essential approach [1]. Then, optical access networks to connect many antennas for the small cells to a central node become important [2]. Another background is that expansion of broadband applications and diversification of user devices are bringing various requirements to the network. To accommodate such various requirements on demand, it is needed make it easier to add and replace functions in access network equipment [3]. In addition to address these two issues, it is important to think about how to further increase the basic performance of optical access networks to prepare to any future upgrades. The following sections review recent researches from these three aspects.

2. Optical access for the mobile fronthaul (MFH)

Centralized Radio Access Network (C-RAN) architecture is considered as a valid solution to support a sustainable growth of the mobile access in the 5th generation mobile communications [4, 5]. In the C-RAN architecture, An Remote Radio Head (RRH) is located at each remote antenna site while baseband processing of the wireless transmission is centralized into Base Band Units located at a central node. The section between the RRHs and the BBUs is called Mobile Front-Haul (MFH).

Optical access is the primal solution to realize the MFH in terms of providing high and stable performance in the 5G RAN, in which several Gbit/s to 10 Gbit/s speed is assumed in the wireless communication [1]. Passive Optical Network (PON) systems provide point-to-multipoint (PtMP) fiber connections in a cost effective manner, so they can effectively support small cells especially when they are densely deployed. Thus, various studies have been reported on how to apply PON technologies to MFH [6-9].

One of the focuses among such studies is cooperation between optical systems and mobile wireless systems to maximize the performance in total. Figures 1 illustrates such cooperation in the dynamic bandwidth allocation [6]. As shown in the figure, the Optical Line Terminal (OLT) at the center node in PON dynamically allocates bandwidth to each Optical Network Unit (ONU) at the antenna side while the BBU dynamically allocates bandwidth to each User Equipment (UE). By sharing the allocation information from the BBU to the OLT in real time, the OLT can allocate bandwidth to each ONU in just proportion in advance to the arrival of the corresponding upstream signals. This method can minimize the latency in the upstream transmission in the network. Another example of such cooperation is that in the power-saving control; a method has been reported to minimize the latency by coordinating the ONU-sleep control in PON with the discontinuous reception (DRX) to save power in UE in the mobile system [7].

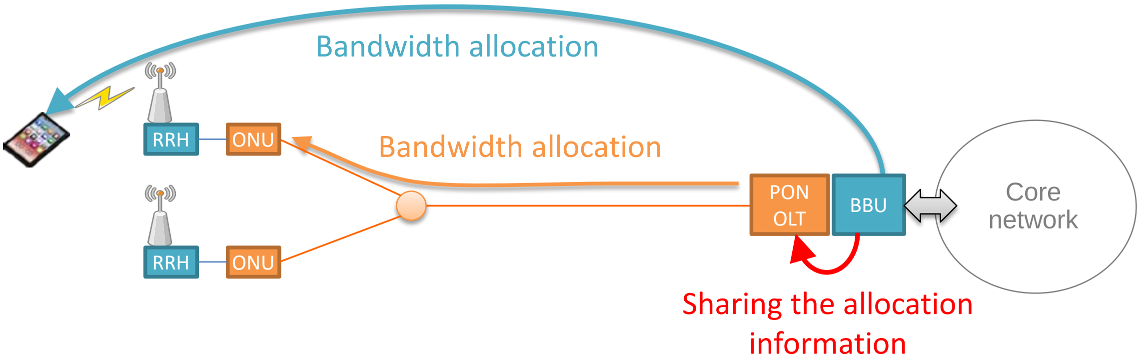

Figure 1 – Cooperation between optical and mobile wireless systems; (a) cooperative bandwidth allocation and (b) cooperative power-saving control

3. Modularization and virtualization

Expansion of broadband applications and diversification of user devices are bringing various requirements to the network. However, in the current systems, it is not easy to add or replace functions to accommodate new service requirements on demand. Access network modularization and virtualization are the keys to address this issue. Figures 2(a) and 2(b) show the first step and the second step of the evolutions in a view [3]. In the first step, access network functions are implemented as software modules with common interfaces so that each function can be added or replaced depending on requirements. This approach can be applied in the current network. In the second step, some of the functions are "virtualized," i.e. moved to the cloud. This can happen in the era of Software Defined Network (SDN) in future. In addition, deeper softwarization will further increase the flexibility and potentially realize "fully programmable" optical access.

Related works include Central Office Re-architected as Datacenter (CORD) promoted by ON.Lab and several industry players including AT&T [10], Flexible Access Network Architecture (FASA) announced by NTT [11, 12], and Future-X Network announced by Nokia Bell Labs [13]. Within the above-mentioned purpose, FASA relatively focuses on the modularization while CORD relatively focuses on the virtualization.

Challenges for the deeper softwarization include real-time implementation of 10-Gbit/s-class Forward Error Correction and Encryption [14] as well as that of the Multi-Point MAC Control (MPMC) function in an Ethernet PON system [15].

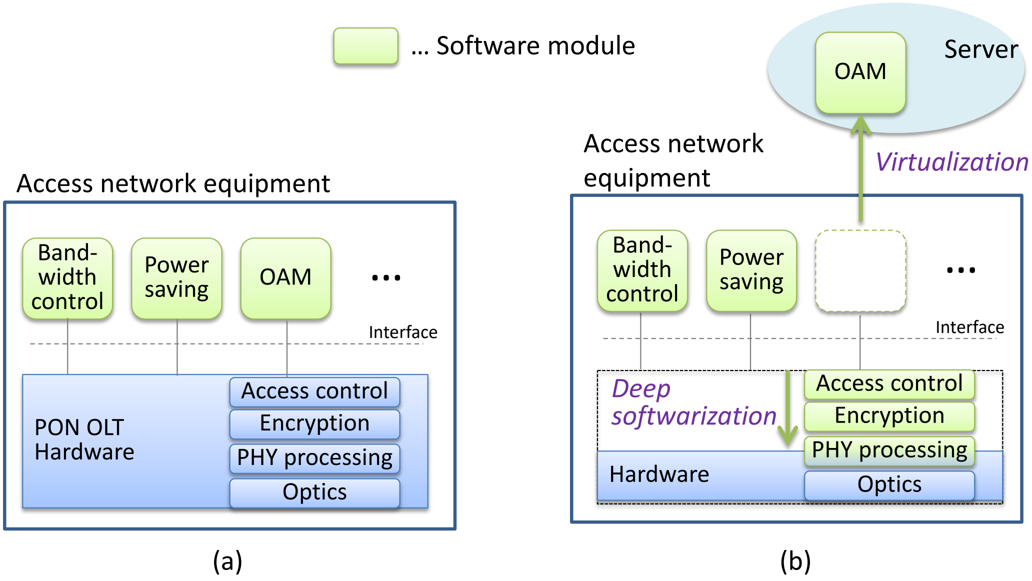

Figure 2 – Access network modularization and virtualization; (a) step 1 and (b) step 2

4. Basic performance increase

Researches to increase the basic performance, e.g. capacity and reach, in optical access are continuously active as well. Such researches will guarantee any upgrades of optical access systems including the new directions mentioned above. Enhancing the peak rate (per wavelength channel) to more than 10 Gbit/s is one of the near-term targets [16].

Among various technical items, how we can use the digital-coherent transmission and reception technologies in optical access is one of the active study topics [17-22]. It has been reported that we can apply the digital-coherent transmission and reception in the burst-mode upstream transmission in PON through implementing a burst-mode optical pre-amplifier and some appropriate digital signal processing functions [22].

References

[1] T. Asai, "5G Radio Access Network and its Requirements on Mobile Optical Network," proceedings of 2015 International Conference on Optical Network Design and Modeling (ONDM), pp. 7-11, 2015.

[2] J. Kani, S. Kuwano, J. Terada, "Options for future mobile backhaul and fronthaul," Optical Fiber Technology, Vol. 26, pp. 42-29, 2015.

[3] J. Kani, "Solutions for future mobile fronthaul and access-network convergence," OFC2016, paper W1H.1, Mar. 2016..

[4] K. Kiyoshima et al, "Commercial Development of LTE-Advanced Applying Advanced C-RAN Architecture – Expanded Capacity by Add-on Cells and Stable Communications by Advanced Inter-cell Coordination," NTT DOCOMO Technical Journal, Vol. 17, No. 2, pp. 10-18, 2015.

[5] C.-L. I, J. Huang, R. Duan, C. Cui, J. Jiang, L. Li, "Recent Progress on C-RAN Centralization and Cloudification," IEEE Access, Vol. 2, pp. 1030-1039, 2014.

[6] T. Tashiro, S. Kuwano, J. Terada, T. Kawamura, N. Tanaka, S. Shigematsu, and N. Yoshimoto, “A Novel DBA Scheme for TDM-PON based Mobile Fronthaul,” OFC2014, paper Tu3F.3, Mar. 2014.

[7] N. Iiyama, J. Kani, J. Terada, N. Yoshimoto, “A study on cooperation of sleep control and DRX control in mobile fronthaul based on TDM-PON,” IEICE General Conference, B-8-55, Niigata, March, 2014 (in Japanese).

[8] A Pizzinat, P. Chanclou, F. Saliou, T. Diallo, “Things you should know about fronthaul,” IEEE J. Lightwave Technol. Vol. 33, pp. 1077-1083, 2015.

[9] N. Shibata, T. Tashiro, S. Kuwano, N. Yuki, J. Terada and A. Otaka, “Mobile front-haul employing Ethernet-based TDM-PON system for small cells,” OFC2015, paper M2J.1, Mar. 2015.

[10] Larry Peterson, IEEE Software Defined Networks - Newsletter, “CORD: central Office Re-architected as a Datacenter (CORD),” November 2015.

[11] NTT press release, “Introducing the New FASA Concept for Future Access Systems – With access equipment modularization, NTT enables service providers to begin service immediately –,” Feb 2016: http://www.ntt.co.jp/news2016/1602e/160208a.html

[12]NTT Access Network Service Systems Laboratories, “Flexible Access Network Architecture – White Paper,” May 2016: http://www.ansl.ntt.co.jp/e/global/FASA/index.html

[13] “The Future X Network – A Bell Labs Perspective,” CRC Press, March 2016.

[14] T. Suzuki, S.-Y. Kim, J. Kani, K.-I. Suzuki, A. Otaka, T. Hanawa, “Parallelization of Cipher Algorithm on CPU/GPU for Real-time Software-Defined Access Network,” Proceedings of APSIPA Annual Summit and Conference 2015, pp. 484-487, Dec 2015.

[15] K. Nishimoto, M. Tadokoro, T. Mochida, A. Takeda, T. Tanaka, and T. Inoue, “Virtualization of EPON OLT functions and collision suppression techniques for Multi-Point MAC Control,” Optical Fiber Communication Conference, OSA Technical Digest (Optical Society of America, 2016), paper W3F.1, 2016.

[16] P. P. Iannone, A. H. Gnauck, D. T. van Veen, and V. E. Houtsma, “Increasing TDM Rates for Access Systems Beyond NG-PON2,” J. Lightwave Technol. 34, 1545-1550, 2016.

[17] N. Yoshimoto, J. Kani, S. -Y. Kim, N. Iiyama, J. Terada, “DSP-based optical access approaches for enhancing NG–PON2 systems,” Commun. Mag., Vol. 51, No. 3, pp. 58–64, 2013.

[18] H. Rohde, E. Gottwald, S. Rosner, E. Weis, P. Wagner, Y. Babenko, D. Fritzsche, H. Chaouch, “Trials of a Coherent UDWDM PON Over Field-Deployed Fiber: Real-Time LTE Backhauling, Legacy and 100G Coexistence,” J. Lightwave Technol. Vol. 33, pp. 1644-1649, 2015.

[19] J. Prat, I. Cano, M. Presi, I. Tomkos, D. Klonidis, G. Vall-llosera, R. Brenot, R. Pous, G. Papastergiou, A. Rafel, E. Ciaramella, “Technologies for cost effective udWDM-PONs,” IEEE J. Lightwave Technol., vol. 34, no. 2, pp. 783-791, 2016.

[20] S. -Y. Kim, J. Kani, K. -I. Suzuki, A. Otaka, “OLT Receiver for Power Normalization of Burst OFDM Signals Enabling OFDM/TDMA-PON,” Photon. Technol. Lett., Vol. 26, No. 24, pp. 2469-2472, 2014.

[21] S.-Y Kim, N. Iiyama, J. Kani, R. Koma, T. Suzuki, K.-I. Suzuki, A. Otaka, “Real-time demonstration of 30

Gbit/s hierarchical star 8-QAM passive optical network employing fractionally-spaced signed-error radius directed equalization," IET Electron. Lett., Vol. 52, No. 7, pp. 544-546, 2016.

[22] R. Koma, M. Fujiwara, J. Kani, S. -Y. Kim, T. Suzuki, K. -I. Suzuki, A. Otaka, H. Mori, T. Wada, "22-dB Dynamic Range, Real-Time Burst-Mode Reception of Digital Coherent 20-Gb/s QPSK PON Upstream Signals," ECOC2016, Presentation M.1.E.4, Sept 2016.

D8. Optical Access Networks for broadband IoT services

Naoto Yoshimoto
Chitose Institute of Science and Technology

I. INTRODUCTION

Recently, wired-wireless converged networks with sensors have been eagerly investigated to provide various cloud services using big data handling techniques [1] [2]. Video monitoring is a kind of attractive wireless sensors. High definition video technology such as 4K has been drastically developed and various 4K cameras are widely diffused. Since such high quality video cameras can be monitored human activities and traffic condition clearly, it will be expected to construct secure and safety community toward future IoT era. Although high definition video cameras constantly output large size of data (giga-bit class), quite efficient data compressed technique for high definition video data such as H.265/HEVC has been progressed [3]. Therefore, we can transmit data of 4K video camera compressed to moderate capacity (mega-bit class). In this report, Distributed 4K-Video camera monitoring on already deployed Ethernet PON (Passive Optical Network) system is proposed. This is some advantage. The first is cost-effectiveness. Since 1G- Ethernet PON (1G-EPON) has massively been installed, it is easily and quickly utilized for new broadband services. The second is upgradability to 8K and uncompressed signal compared with wireless access such as Long Term Evolution (LTE), because PON system has authorized upgrade scenario toward 10G-Ethernet PON (10G-EPON) and Next-generation PON-2 (NG-PON2). The third is capability of service co-existence with current provided broadband services such as WiFi spot service. In broadband service, downstream traffic is generally large than upstream one. On the other side, in 4K-video monitoring service, upstream traffic is large than downstream one. Therefore, bandwidth can be efficiently used at not only downstream and but also upstream. Figure 1 shows an image of secure and ubiquitous community based on optical access network using widely distributed 4K video cameras. 4K video cameras are located in the office area and residential area as well as WiFi base stations (for outside Internet service), and are connected with optical fiber cable deployed for FTTH (Fiber to the Home).

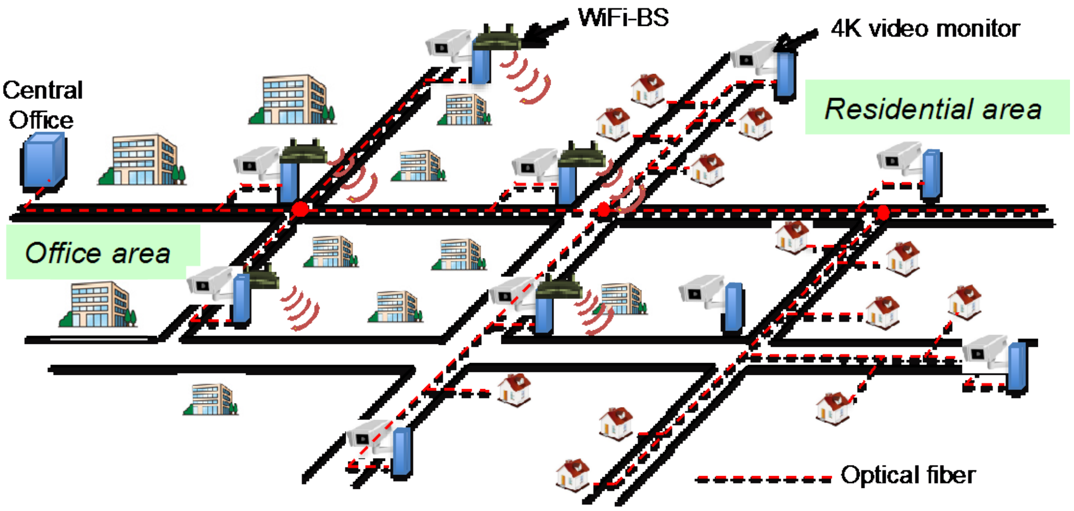

Fig.1 Secure and ubiquitous community based optical access network widely distributed 4K video monitors and WiFi base station

II. NETWORK CONFIGURATION

Figure 2 shows proposed 4K video monitoring and data transmission system based on 1G-EPON. Service area is up to 10 km as typical size of community and number of connected 4K video monitors is up to 32 as equal to typical splitting ratio of 1G-EPON systems. At the 4K-transmitter, compressed 4K video data is packetized and transmitted through gigabit Ethernet interface with variable frame size in accordance with traffic condition and buffering capacity. Since the data direction is mainly upstream, at the Optical Network unit (ONU), packetized 4K video data should be burst mode transmission on the Time-Division Multiplexing Access (TDMA). The burst cycle is set to 10 msec and the data load is controlled by changing the burst size flexibly as shown in the inserted right side block in Fig.2. In PON span, the upstream packets are controlled by the both fixed and dynamic bandwidth allocation technique.

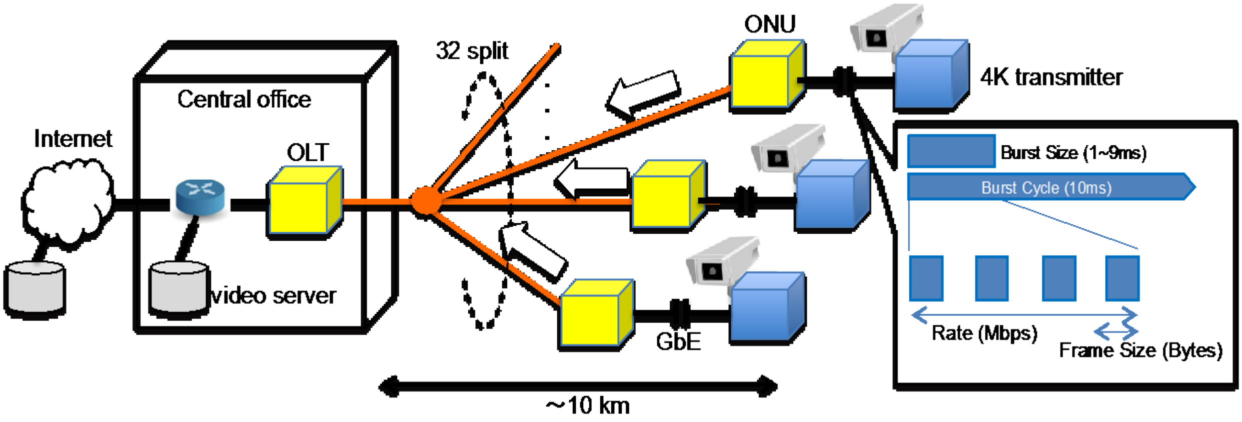

Fig.2 4K video monitoring and transmission system based on 1G-EPON

III. SIMULATION

In order to confirm the feasibility of the proposed network configuration for 4K-video monitoring service, we evaluated the performance of 1G-EPON systems by using PON traffic simulation “SimOliver.”

Table 1 Simulation parameter of 4K monitoring and Internet service

Service	Priority	Bit rate	Frame size
4K monitoring	high	upstream 30 Mbps	upstream fixed 1518 Byte
Internet (WiFi spot)	low	upstream 1.5 Mbps downstream 20 Mbps	up/downstream random 64-1518 Byte

The simulation parameters of 4K video monitoring service and Internet service are listed in Table 1. The queue set had two priorities; the data traffic of 4K-video monitoring service is assigned to “high priority” and that of Internet service is assigned “low priority.” The bandwidth for high priority was reserved to 15 Mbps. The upstream data rate of 4K-video is set to 30 Mbps according to the typical transmission rate of compressed 4K video data by H.265. The flame size of the upstream data was fixed to 1518 Byte to easily control bandwidth allocation at the PON system for efficient transmit thorough the PON span. On the other side, the upstream and downstream data rate of Internet service was set to 1.5 Mbps and 30 Mbps, respectively, which values is according to the typical transmission rate of Internet service. The flame sizes of the both directions were varied from 64 to1518 Byte randomly.

Firstly, a case of dedicated 4K-video service (all 32 ONUs are connected to 4K-video) was simulated. Figure 3 shows the simulated result of mean packet delay as a function of network load. At this case, Fixed Bandwidth Allocation (FBA) mode is more suitable, because only 4K-video traffic continuously transmitted and the frame size was set to fixed value at the 4K-transmitter as mentioned above. As the network load increased, the mean packet delay gradually increased, and the network load exceeded to 0.8, the delay rapidly increases. As a result, the burst packet interval should be controlled as equal to the network load of less than 0.8. Secondly, a case of shared 4K-video service (32 ONUs are connected to 4K-video and the additional ONUs are connected to Internet service) was simulated for multiple service coexistence.

Figure 4 shows the simulated result of mean packet delay as a function of connected Internet service users on the same PON branch. In this simulation, there are four types of bandwidth allocation scheme as listed in Fig. 4. The Priority Dynamic Bandwidth Allocation (P-DBA) means that 4K-video service is set priority and the total bandwidth is assigned by DBA mode. On the other hand, the Non Priority DBA (Non P-DBA) means that both services are fairly treated and the total bandwidth is assigned by DBA mode. P-FBA and Non P-FBA shows that the total bandwidth is assigned by FBA mode. As shown in Fig. 4, even priority based FBA, the value of the mean packet delay was high, because the traffic pattern of Internet service is assumed to be random access, not to be fixed rate access. By using DBA mode, as the number of Internet user increased, the mean packet delay was still low. Therefore, in case of both 4K-video and Internet service provisioning, DBA mode is more suitable for highly efficient traffic management. In such way, hybrid bandwidth allocation scheme by using both FBA and DBA according to various service provisioning and traffic condition is valuable for multiple service access networks in near future.

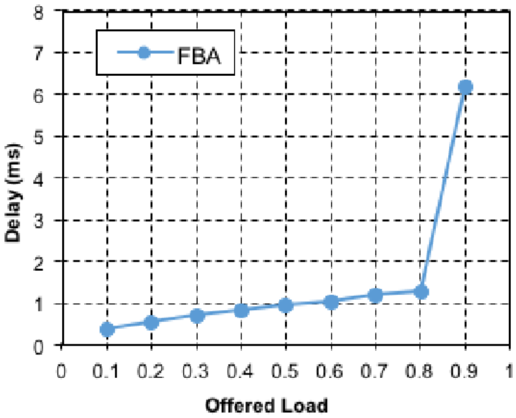

Fig.3 Simulated result of mean packet delay in case of dedicated 4K-video **monitoring service**

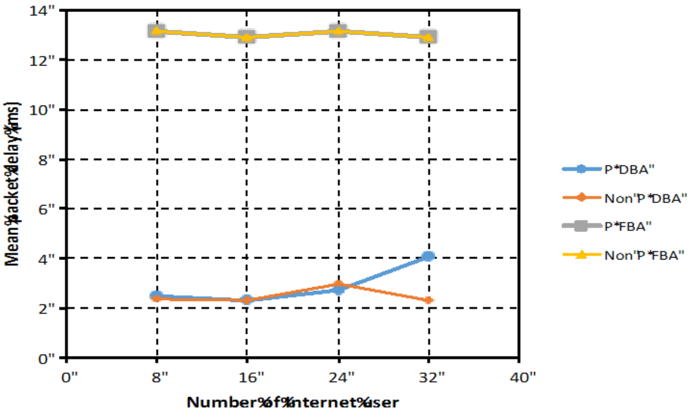

Fig.4 Simulated result of mean packet delay of 4K-video monitoring service in **case of shared with Internet service as a function of number of Internet user**

References

[1] N. Yoshimoto, “Operator Perspective on Next-Generation Optical Access for High-Speed Mobile Backhaul,” OFC2013, OTu3E.1, March 2013.

[2] K. Iwatsuki and K. Tsukamoto, “Next-generation resilient access networks,” Proc. SPIE VOl. 9387, pp. 9387-2-1-8, San Francisco, CA, February 2015.

[3] M. Ikeda, “H.265/HEVC encoder for UHDTV,” 20th Asia and South Pacific Design Automation Conference (ASP-DAC2015), pp. 686-688, Chiba, Japan, January 2015.

D9. Construction of resilient cyber physical system based on ICT

Katsumi Iwatsuki
Tohoku University

ABSTRACT

While development of science and technology has built up the sophisticated civilized society, it has also resulted in quite a few disadvantages in global environment and human society. The common recognition has been increasingly shared worldwide on sustainable development society attaching greater importance to the symbiotic relationship with nature and social ethics. After the East Japan Great Earthquake, it is indispensable for sustainable social development to enhance capacity of resistance and restoration of society against natural disaster, so called “resilient society.”

Our society consists of various Cyber Physical Systems (CPSs) that make up the physical systems by fusing with an Information Communication Technology (ICT). We describe the proposed structure of CPS in order to realize resilient society. The configuration of resilient CPS consisting of ICT and physical system is discussed to introduce “autonomous, distributed, and cooperative” structure, where subsystems of ICT and physical system are simultaneously coordinated and cooperated with Business Continuity Planning (BCP) engine, respectively. We show the disaster response information system and energy network as examples of BCP engine and resilient CPS, respectively. We also propose the structure and key technology of resilient ICT.

Keywords: Cyber physical system (CPS), Business Continuity Planning (BCP), Resilience, Network Function Virtualization (NFV), Software Defined Network (SDN), Full coherent transmission technology, Wavelength division multiplexing Passive optical network (WDM-PON)

INTRODUCTION

Though natural disasters as yet unpreventable, the key issue in the conventional disaster management study has been improving disaster resistance. Disaster prevention technology of course has its own limitations. Recently, attention has been increasingly paid to disaster mitigation technology based on the idea that upon the occurrence of a disaster, restoration and reconstruction should be conducted swiftly and effectively to minimize adverse impact due to disasters. To realize sustainable social development, it is indispensable to enhance capacity of resistance and restoration of society against disaster by combing the disaster prevention technology and disaster mitigation technology. We name the society resilient to disaster “Resilient Society” [1].

By fusing with the Information Communication Technology (ICT), a physical system becomes smarter as a Cyber Physical System (CPS). Our society consists of various CPSs based on the physical systems X_i, such as transportation, robot, energy network, city, and so on, as shown in Fig.1. To realize resilient society, we need to improve resilience of CPS itself with introducing the autonomous, distributed, and cooperative operation, and simultaneously to coordinate and cooperate each CPS with a business continuity planning (BCP) engine, as shown in Fig.2.

Figure 1. Social system consisting of various cyber physical systems (ICT x X_i).

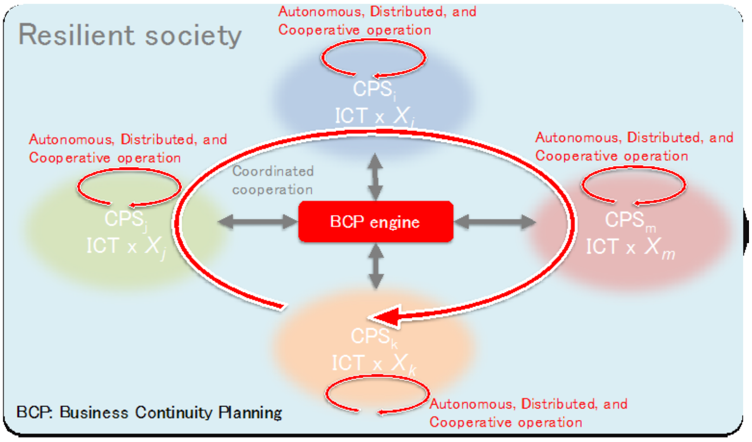

Figure 2. Resilient society realized with resilient CPS.

When the disaster occurs, we lose and recover the function and performance of system as shown in the red line of Fig. 3. The function and performance changes over the time as shown in blue line of Fig. 3, with improving resilience of system. The framework of resilience in Ref. [2] shows that four fundamental properties, “Robustness”, “Redundancy”, “Resourcefulness”, and “Rapidity” in Fig. 3 are required to achieve the resilience. The approach to four fundamental properties is as follows:

- Approach of Robustness; we make elements and/or subsystems composed of system stronger against a disaster. The autonomous system can achieve Robustness.
- Approach of Redundancy; we don’t aggregate functionality of system in one place. The distributed system can achieve Redundancy.

- Approach of Resourcefulness and Rapidity; we configure the system again with resources that are inserted from the outside. The cooperative operation of system easily to insert the resources can achieve Resourcefulness and Rapidity.

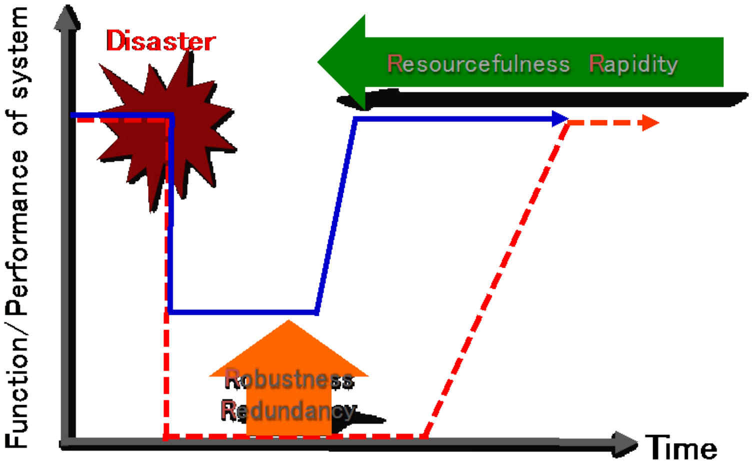

Figure 3. Four fundamental properties to achieve resilience.

REALIZATION OF RESILIENT CYBER PHYSICAL SYSTEM

The CPS consists of ICT and physical system X_i. The ICT and X_i are composed of subsystem of ICT_n and X_{in} (n = I, j, k, m), respectively, as shown in Fig. 4. Among ICT_n and X_i, the information and physical quantity of χ , for example current in power grid, is distributed, respectively. To realize the resilient CPS, the four fundamental properties are achieved with introducing autonomous, distributed, and cooperative operation to both ICT_n and physical system X_{in}. Subsystems of ICT_n and X_{in} simultaneously are coordinated and cooperated with a Business Continuity Planning (BCP) engine, respectively, as shown in Fig.4. The BCP engine collects and analyzes environmental data, so as to grasp the disaster situations and operating condition of ICT_n and X_{in}.

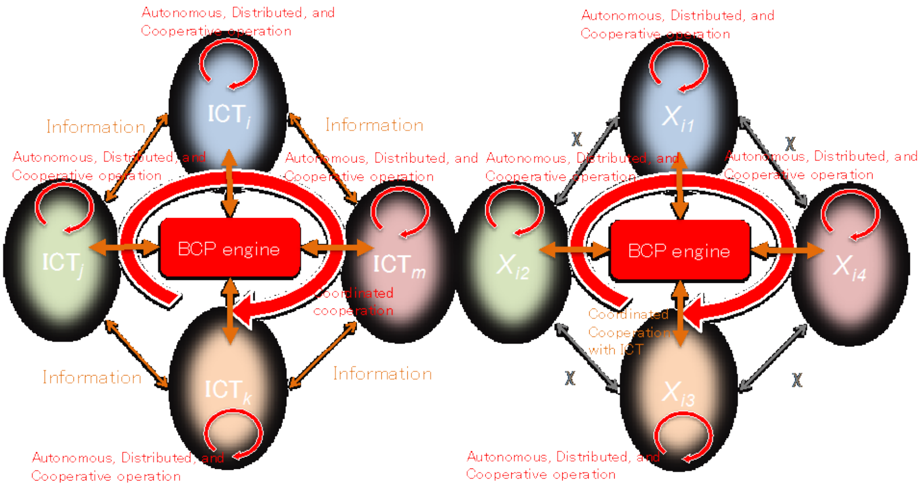

Figure 4. Configuration of resilient CPS.

Figure 5 shows the conceptual diagram of BCP engine to support the resilient society. Various data from broadcasting, social media, Xi with sensors are gathered through network as big data. The big data are analyzed with information technologies, such as deep learning, natural language processing, speech recognition, and so on, and then we can understand operating conditions of CPSs with the visualized information from BCP engine by smart devices.

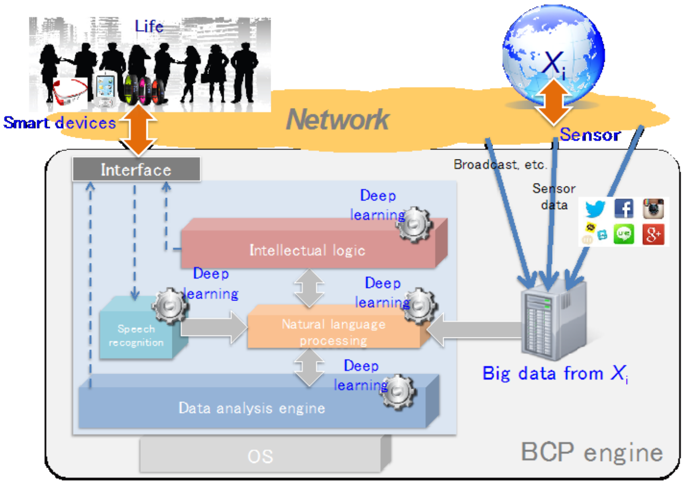

Figure 5. Conceptual diagram of BCP engine to support the resilient society.

We introduce the disaster response information system in Fig.6, as an example of BCP engine. As for the disaster response against the East Japan Great Earthquake, inefficient disaster-information gathering and sharing based on papers is a critical issue. To prepare the Tokyo Metropolitan Earthquake and Tokai-Tonankai-Nankai Earthquake, predicting the occurrence in near future, the development of information systems to support disaster response and recovery will be an urgent issue. To make efficiently a database of disaster information and response record, and to utilize effectively the information and accumulate lessons for future by analyzing the huge database, we apply the natural language processing and speech recognition technologies, so that computers assist to structure various kinds of disaster information and automatically make the database, as shown in Fig. 6. Then, we solve the bottleneck of disaster-information input into the database with keyboard in actual work, so as to share the accurate and quick recognition of present situation in the case of disaster [3].

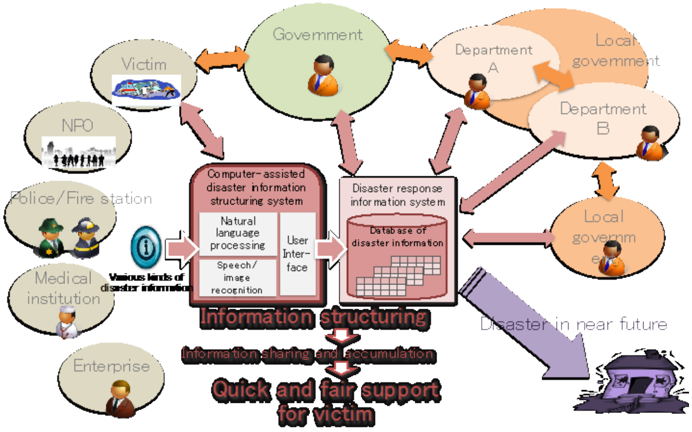

Figure 6. Disaster response information system.

We also introduce the resilient energy network in Fig.7 [4], as an example of resilient CPS. The fundamental of power grid is multi-port power routers, which joint solar panels, batteries, and households with having small solar panels and batteries, as a ring topology. The router is composed of three-way isolated DC/DC converter as a core unit and AC/DC converter units. The router can distribute power in three directions and perform the power interchanging function regardless of DC and AC, with the use of resilient ICT. In the usual time, the surplus electricity in the power grid is lent to power-shortage households. In the time of disaster, each household is operating with self-sufficient power supply or power supply from surviving power grid.

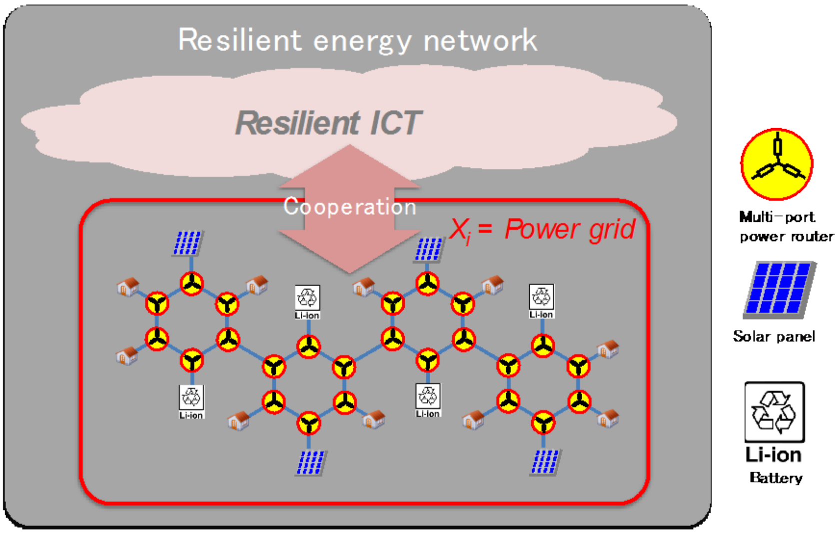

Figure 7. Resilient energy network.

REALIZATION OF RESILIENT ICT

Figure 8 shows whole picture of resilient ICT. Environmental data from sensor networks are analyzed with the distributed cloud computing which operates as the BCP engine, so as to grasp the information of disaster situations and operating conditions of networks, such as wireless network, Wi-Fi network, ITS network, Ad-hoc network, and so on. Using the information from the distributed cloud computing, we can autonomously and cooperatively operate various networks, even in the time of huge disaster, and then we can enhance resilience of networks.

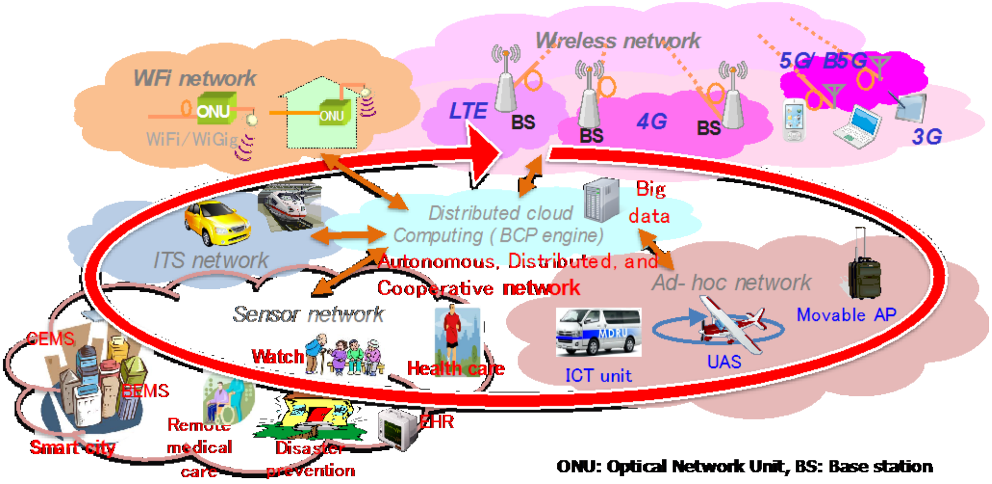

Figure 8. Whole picture of resilient ICT.

Since existing wired and wireless access networks have been constructed independently, we cannot cooperatively operate wired and wireless access networks, and then the resilience is insufficient. The key technology of cooperative operation of networks is to virtualize into the physical layer with "full coherent transmission" together with the Network Function Virtualization (NFV) and/or Software Defined Network (SDN) of access networks, as shown in Fig. 9 [5].

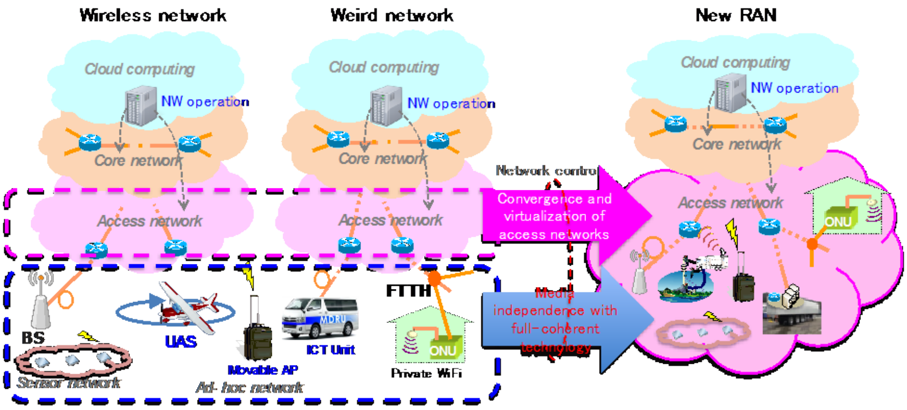

Figure 9. Resilient network with technical convergence of wired and wireless.

Optical transmission technologies

Figure 10 shows the configuration of NG-PON2. NG-PON2 is constructed based on WDM-PON, which is a physically shared system, but a logically unshared system. Several wavelengths of WDM-PON are adapted for TDM-PON. The other wavelengths of WDM-PON are used as point-to-point WDM. The wavelength allocation of WDM is going to be standardized in Full Service Access Network (FSAN). The point-to-point WDM can be applied to accommodate broadband mobile access networks.

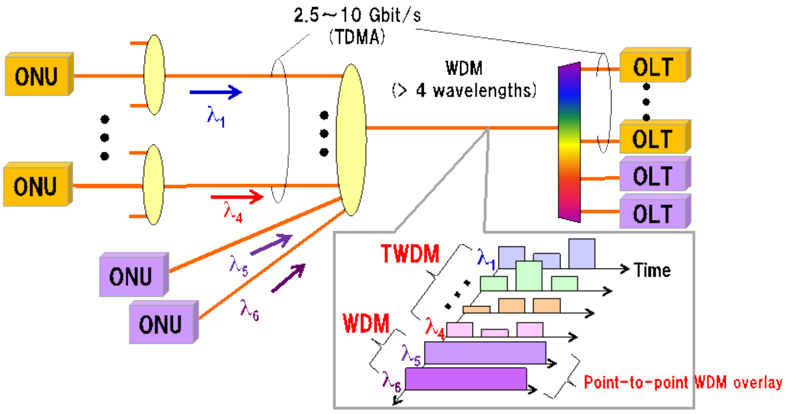

Figure 10. Configuration of NG-PON2.

Figure 11 shows the fundamental configuration of digital coherent optical transmission. The optical wave emitted from coherent light source is modulated by QAM signals with an IQ modulator. The modulated optical wave is transmitted through an optical fiber, and then homodyne detection is achieved with a coherent receiver and local oscillator. The transmitted signal is demodulated with an analog digital converter (A/D) and digital signal processor.

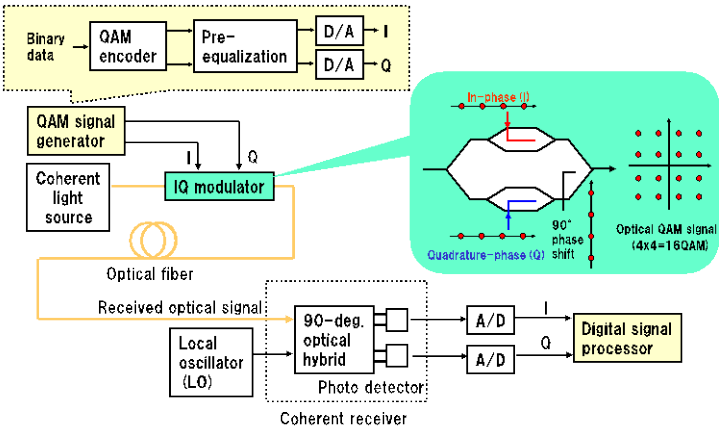

Figure 11. Fundamental configuration of digital coherent optical transmission.

Wireless transmission technologies

Figure 12 shows the rapid increase of mobile traffic over the past time and also the prediction in near future. The mobile traffic of 5G commercially starting at 2020 is predicted more than1000 times as compared with that of 3G. The main traffic after LTE system is data and video downloaded from the cloud through the internet. So, we will develop technologies for 5G mobile networks to accommodate a huge traffic. One of the most promising approaches is to achieve a small cell with distributed antenna network (DAN), as shown in Fig. 13 [6]-[9]. A large number of antennas are distributed and covered in the existing a macro cell, and many antennas are accommodated in several signal processing centers (SPCs) with optical links. Each SPC is connected with optical links as well. The issue of DAN is how to cost-effectively and flexibly achieve a lot of antennas and optical links connecting between each antenna and SPC.

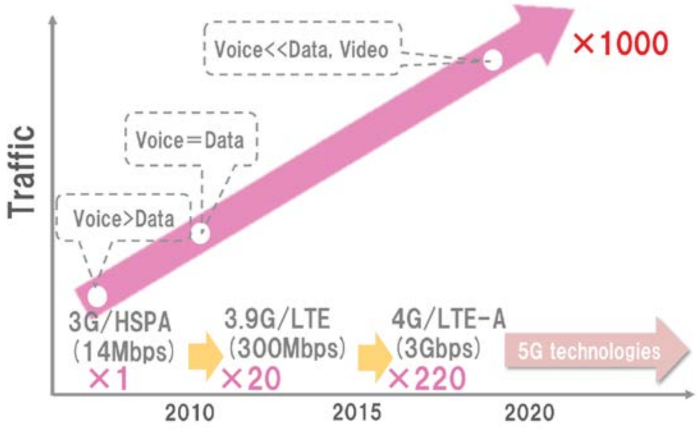

Figure 12. Rapid increase of mobile traffic.

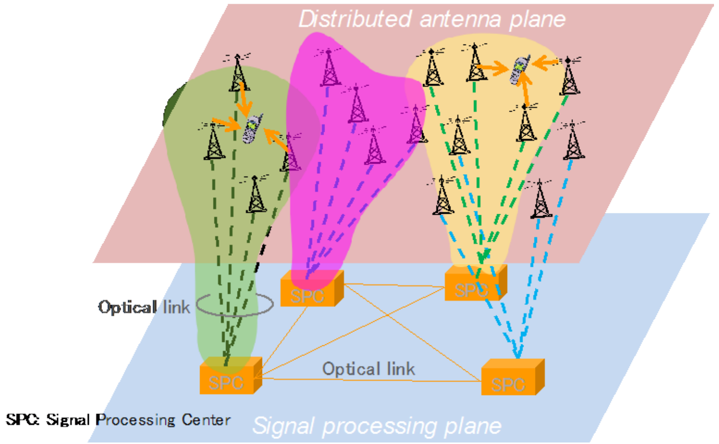

Figure 13. Realization of small cell with distributed antenna network.

Convergence of wired and wireless with coherent technology

We can adopt same modulation format as wireless transmissions for optical fiber transmissions with developing the digital coherent technology. When we apply frequency convertor from optical to wireless carrier with preserving the carrier coherence, optical signals transmitting through optical fibers can be radiated from an antenna as wireless signals, as shown in Fig. 14. We call this technology "full coherent transmission." The media independent transmission can be achieved with the full coherent transmission, so that we will construct cost-effective and flexible access networks together with the SDN and/or NFV.

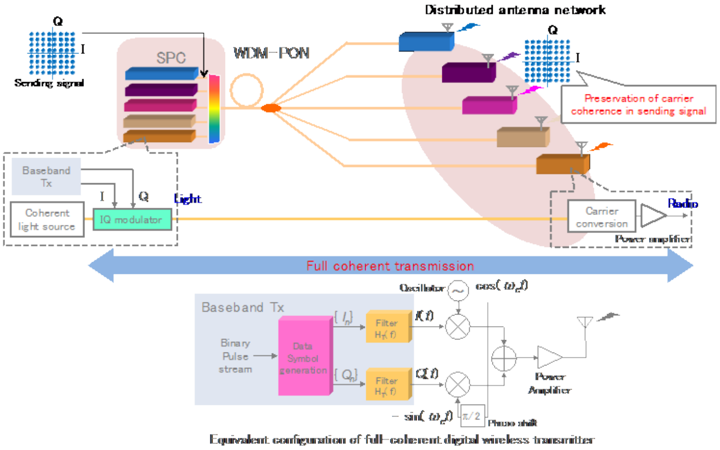

Figure 14. Full coherent technology with convergence of wired and wireless.

SUMMARY

We described the proposed structure of resilient CPS consisting of ICT and physical system in order to realize resilient society. The configuration of resilient CPS was discussed to introduce “autonomous, distributed, and cooperative” structure into both ICT and physical system, where subsystems of ICT and physical system are simultaneously coordinated and cooperated with BCP engine, respectively [10]. We showed the disaster response information system and resilient energy network as examples of BCP engine and resilient CPS, respectively. With the use of the information analyzing data from sensor, broadcasting and social media, we can autonomously and cooperatively operate various networks, so as to realize the resilient ICT. We also described the key technology of resilient ICT to virtualize into the physical layer with full coherent transmission with convergence of wired and wireless.

ACKNOWLEDGEMENT

The author is grateful thanks to Profs. F. Adachi, M. Nakazawa, N. Kato, and Associate Prof. H. Nishiyama of Tohoku University, and Prof. Y. Kado of Kyoto Institute of Technology for their fruitful discussions.

REFERENCES AND LINKS

[1] K. Iwatsuki, and H. Hayashi, “The Realization of Resilient Society with Information Technology Revolution,” J. Disaster Research, Vol.5 No.6, pp.622-626, 2010.

[2] https://mceer.buffalo.edu/meetings/AEI/presentations/01Bruneau-ppt.pdf

[3] K. Iwatsuki, “The projects of disaster-resistant information communication network at the Research Organization of Electrical Communication, Tohoku University,” Proc. of SPIE, Vol.8646, No.86460B, *invited paper*, SPIE Photonics West 2013, 8646-9, 2013.

[4] Y. Kado, K. Iwatsuki, and K. Wada, “Multi-port power router and its impact on resilient power grid systems,” Proc. of SPIE, Vol.9772, No. 9772-18, *invited paper*, SPIE Photonics West 2016, 2016.

[5] K. Iwatsuki and K. Tsukamoto, “Next Generation Resilient Access Networks,” *invited paper*, SPIE Photonics West 2015, San Francisco, vol.9387, p.93870J-1, 2015.

[6] F. Adachi, “Wireless Optical Convergence Enables Spectrum-Energy Efficient Wireless Networks,” Proc. 2014 International Topical Meeting on Microwave Photonics/the 9th Asia Pacific Microwave Photonics (MWP/APMP 2014), pp.51-56, Sapporo, Japan, 20-23 Oct. 2014.

[7] F. Adachi, et al, “Distributed Antenna Network for Gigabit Wireless Access,” International Journal of Electronics and Communications (AEUE), Elsevier, Vol. 66, Issue 6, pp.605-612, 2012.

[8] F. Adachi, et al, “Recent Advances in Single-carrier Distributed Antenna Network,” Wireless Communications and Mobile Computing, Vol.11, Issue 12, pp.1551–1563, Dec. 2011.

[9] F. Adachi, et al, “Recent Advances in Single-carrier Frequency-domain Equalization and Distributed Antenna Network,” IEICE Trans. Fundamentals, Vol.E93-A, No.11, pp.2201-2211, Nov. 2010.

[10] K. Iwatsuki, “Cyber physical system based on resilient ICT,” *invited paper*, SPIE Photonics West 2016, San Francisco, vol.9772, p.9772-17, 2016.